

UNIFORM ATMOSPHERIC RETRIEVAL ANALYSIS OF ULTRACOOL DWARFS II: PROPERTIES OF 11 T-DWARFS

MICHAEL R. LINE

School of Earth & Space Exploration, Arizona State University, Tempe AZ 85287, USA

MARK S. MARLEY

NASA Ames Research Center, Mail Stop 245-3; Moffett Field, CA 94035, USA

MICHAEL C. LIU

Institute for Astronomy, University of Hawaii, 2680 Woodlawn Drive, Honolulu, HI 96822, USA

CAROLINE V. MORLEY

Department of Astronomy, Harvard University, Cambridge, MA 02138, USA and
NASA Sagan Fellow

BEN BURNINGHAM

Centre for Astrophysics Research, School of Physics, Astronomy and Mathematics, University of Hertfordshire, Hatfield AL10 9AB, UK
and
Marie Curie Fellow

NATALIE R. HINKEL

Department of Physics & Astronomy, Vanderbilt University, Nashville, TN 37235, USA

JOHANNA TESKE

Carnegie Observatories, 813 Santa Barbara Street, Pasadena, CA 91101 and
Carnegie Origins Fellow, jointly appointed by Carnegie DTM & Carnegie Observatories

JONATHAN J. FORTNEY

Department of Astronomy and Astrophysics, University of California, Santa Cruz, CA 95064
Submitted to the Astrophysical Journal

ABSTRACT

Brown dwarf spectra are rich in information revealing of the chemical and physical processes operating in their atmospheres. We apply a recently developed atmospheric retrieval tool to an ensemble of late T-dwarf (600-800K) near infrared spectra. With these spectra we are able to place direct constraints the molecular abundances of H₂O, CH₄, CO, CO₂, NH₃, H₂S, and Na+K, gravity, thermal structure (and effective temperature), photometric radius, and cloud optical depths. We find that ammonia, water, methane, and the alkali metals are present and well constrained in all 11 objects. From the abundance constraints we find no significant trend in the water, methane, or ammonia abundances with temperature, but find a very strong ($>25\sigma$) increasing trend in the alkali metal abundances with effective temperature, indicative of alkali rainout. We also find little evidence for optically thick clouds. With the methane and water abundances, we derive the intrinsic atmospheric metallicity and carbon-to-oxygen ratios. We find in our sample, that metallicities are typically sub solar and carbon-to-oxygen ratios are somewhat super solar, different than expectations from the local stellar population. We also find that the retrieved vertical thermal profiles are consistent with radiative equilibrium over the photospheric regions. Finally, we find that our retrieved effective temperatures are lower than previous inferences for some objects and that our radii are larger than expectations from evolutionary models, possibly indicative of un-resolved binaries. This investigation and methodology represents a paradigm in linking spectra to the determination of the fundamental chemical and physical processes governing cool brown dwarf atmospheres.

1. INTRODUCTION

Brown dwarf spectra contain a wealth of information about the physical and chemical processes occurring in

their atmospheres. Such processes include, but are not limited to: vertical atmospheric energy balance, disequilibrium chemistry, cloud formation/distribution and subsequent impact on molecular composition, and links to formation and evolution (see Marley & Robinson 2015

¹ Correspondence to be directed to mrline@asu.edu

review). The main diagnostic quantities that provide insight into these processes, that can be obtained directly from a spectrum are: vertical thermal structure, molecular abundances, spectroscopic radius, and cloud properties. Deriving these diagnostic quantities is no simple task. Progress in characterization always involves the interplay between observational and modeling efforts. It is from the comparison with models that we aim to understand the underlying physics and chemistry in substellar atmospheres.

The classic method for interpreting brown dwarf spectra is generating a set of self-consistent radiative-convective-thermochemical equilibrium models to which the data can be compared (Allard et al. 1996, Marley et al. 1996, Tsuji et al. 1996, Burrows et al. 2001). Grids of model spectra are typically generated by varying only a few parameters, usually gravity and effective temperature (Kirpatrick 2005) with all of the physics and chemistry in the atmospheres assumed (e.g., self-consistent radiative equilibrium plus equilibrium chemistry is used to predict the thermal structures and molecular abundances). These models are then interpolated along these dimensions via a chi-squared search until a best fit, or range of best fit parameters are found (e.g., Cushing et al. 2008, Rice et al. 2010, Stephens et al. 2009, Liu et al. 2011). In some cases these two parameters are not enough to adequately explain the spectra. Often times the fits are rather poor making any inference about these quantities and their corresponding uncertainties invalid (Czekala et al. 2015). This suggests that the physical assumptions made within the grid models are not adequate enough to describe the data and that the grid models are underutilizing the full information content of the data. To remedy these issues some modelers chose to add additional physical parameters to their models to accommodate for new assumptions not previously (as of then) taken into account such as disequilibrium chemistry via an eddy diffusivity (Saumon et al. 2006; Stephens et al. 2009) and more sophisticated cloud parameterizations (Ackerman & Marley 2001; Cushing et al. 2008). Furthermore, often-unknown differing assumptions within the various flavors of grid models from different groups, given the same sets of basic parameters, don't agree resulting in inconsistent interpretations of the same datasets (Figure 8, Patience et al. 2012).

Motivated by these shortcomings, Line et al. (2014) & (2015) (Part 1 hereafter) built upon the success of atmospheric retrieval methods applied to Earth (Rodgers 1976, Towney 1996, Rodgers 2000, Crisp et al. 2004), solar system (Conrath et al. 1998, Irwin et al. 2008, Fletcher et al. 2007, Greathouse et al. 2011), and exoplanet atmospheres (Lee et al. 2012; Line et al. 2012;13;; Benneke & Seager 2012; Barstow et al. 2013;14, Waldman et al. 2015a,b) to develop a framework for retrieving the molecular abundances, vertical temperature structure, gravity, and other quantities. Such an approach is agnostic as to the detailed physical and chemical mechanisms governing the atmosphere; rather it allows the data to directly determine the fundamental quantities that impact the spectra, such as the opacities (gases or clouds) and radiative source functions. Part I leveraged the power of benchmark brown dwarf-stellar systems (G1570 and HD3651) of which we know the host star ages, metallicities, and a new dimension, carbon-

to-oxygen ratios (C/O's). The goal of Part I was to demonstrate the feasibility of the approach by retrieving these quantities from the companion brown dwarfs. Assuming co-evolution, the brown dwarfs should have the same ages, metallicities, and C/O's as the host star. With low resolution near infrared SpeX data of G1570D and HD3651b, Line et al. (2015) was able to show that the retrieval method was indeed were able to reproduce these quantities to within the errors, thus validating the approach. They also showed, for the first time, that one could robustly detect the presence of ammonia in near infrared low resolution data, without "seeing" obvious spectroscopic features. This detection demonstrated the power of using a Bayesian approach to detect molecules that would have only otherwise been detected at higher resolution (Canty et al. 2015) or at longer wavelengths (e.g., Saumon et al. 2006; Hubeny & Burrows 2007). Furthermore, they were able to rule out the presence of optically significant clouds within the near infrared photospheres of these objects. Finally, via the retrieved temperature structures we were able to validate the radiative equilibrium assumption commonly made in self-consistent grid models.

To illustrate the differences between "retrieval" and "grid-model" fits we compare a representative best fit retrieval model (e.g., Line et al. 2015) to a representative grid model best fit (Morley et al. 2012) in Figure 1. The grid models are based on Morley et al. (2012) with the spectra being computed on a grid as a function of 4 fairly standard free parameters: effective temperature, gravity, clouds parameterized with an "f-sed" (Ackerman & Marley 2001), and a radius-to-distance scale factor (see Morley et al. 2012 for details). Note that the retrieval fit (red) is significantly better than the grid model fit (blue). More quantitatively, the retrieval produces a chi-square per data-point of 5, whereas the best-fit grid model a chi-square per data-point of 14.5. The retrieval model in Part I included 27 free parameters, much more than the 4 used in the grid model. Are the retrievals justified in using this large number of parameters? We turn to the Bayesian Information Criterion (see Figure 1 caption) which penalizes models with more free parameters. In this case, the retrieval model is overwhelmingly favored, with a BIC difference of ~ 1200 (way off of the Jefferey's scale (e.g., Kass & Raftery 1995)). One potential drawback of the retrieval models is, however, the possibility of unphysical solutions. As shown in Part I, the solutions obtained with our methodology are indeed chemically and physically plausible. We elaborate on this further in a later section.

In this manuscript, Part II, we apply the Part I retrieval methodologies to a small sample (11) of late T-dwarfs (T7-T8) within the SpeX Prism Library (Burgasser et al. 2006a) in order to identify diagnostic physical/compositional trends. We start with the late T-dwarfs as they are presumed to be free of optically thick clouds (and demonstrated on two objects in Part I) (e.g., Marley et al. 1996, Allard et al. 1996), significantly reducing cloud degeneracies with abundances and thermal structures. The long term goal is to extract molecular abundances, thermal structures, cloud properties, etc., for a large number (\sim hundreds to thousands) of objects by working our way up (and down) the brown-dwarf spectral sequence, starting with these late T's then Y-dwarfs,

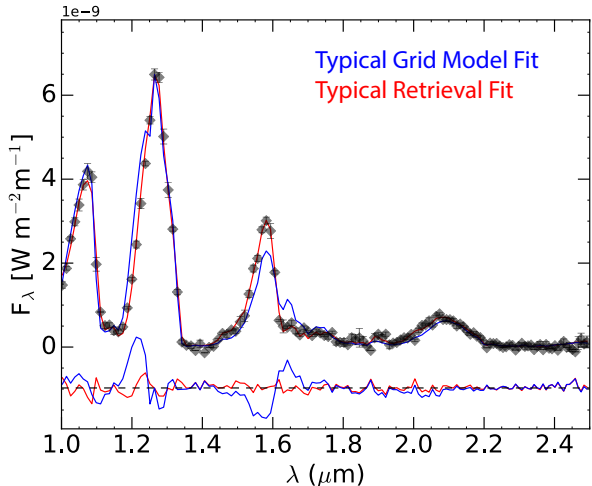


FIG. 1.— Comparison between retrieval fits and self-consistent grid model fits. The fit residuals are shown at the bottom of the plot. The grid model fit (in blue) is based on a standard set of assumptions (e.g., Saumon & Marley 2008; Morley et al. 2012) involving 4 free parameters: the effective temperature, gravity, cloud sedimentation (Ackerman & Marley 2001), and a flux scaling factor. The nominal best fit grid model (effective temperature=900K, log-gravity=5., no cloud) results in a chi-square per data point of 14.5, with 139 data points. With 4 free parameters, this results a Bayesian Information Criterion Value of 2035.2. In contrast the retrieval model (red) with 27 free parameters produces a chi-square per data point of 5.0 and a BIC of 832.4. Despite the factor of 7 in the number of free parameters, the retrieval model is overwhelmingly favored with a ΔBIC of ~ 1200 , which would be considered “Very Strong” on the Jeffery’s scale.

followed by more cloudy mid-to-early T’s and finally L-dwarfs. By investigating “simpler” objects first, we can continue to identify the strengths and weaknesses of our model parameterization, and make the necessary adjustments along the way.

The manuscript is organized as follows: §2 briefly summarizes the methodology outlined in Part I, and identifies small changes, §3 introduces the 11 T-dwarf sample, §4 presents our retrieved quantities and the useful derived diagnostic quantities and trends, and finally in §6 we summarize our findings and discuss implications.

2. METHODS

Here we briefly summarize our methodologies extensively described in Part I. We couple a simple thermal emission radiative transfer forward model (Line et al. 2013a; 2014a,b; 2015) with the powerful EMCEE sampler (Foreman-Mackey et al. 2014). The job of the forward model is to compute the observable, in this case, the disk-integrated top-of-atmosphere thermal flux with wavelength. We neglect scattering due to clouds and treat everything as pure absorption. This assumption may break down in the presence of strongly forward scattering clouds. The inputs into the forward model are the vertically uniform volume mixing ratios for H_2O , CH_4 , CO , CO_2 , NH_3 , H_2S , Na, and K, gravity, temperature-pressure (TP) profile, and the radius-to-distance scaling factor. We use the same novel TP-profile retrieval scheme described extensively in Part I. All other nuisance parameters from Part I are included (see Table 1).

We discuss a few relevant illuminating modeling points not discussed in Part I. Firstly, the the statistics reviewer for Part I suggested we explore the impact of alternate

TABLE 1
FREE PARAMETERS IN THE FORWARD MODEL (31 IN TOTAL)

Parameter ^a .	Description
$\log f_i$	log of the uniform-with-altitude volume mixing ratios of H_2O , CH_4 , CO , CO_2 , NH_3 , H_2S , and alkali (Na+K)
$\log g$	log gravity [cms^{-2}]
$(R/D)^2$	radius-to-distance scaling (R_J/pc)
T_j	temperature at 15 pressure levels (K)
$\Delta\lambda$	uncertainty in wavelength calibration (nm)
b	error bar inflation exponent (Part 1, equation 3)
γ, β^b	TP-profile smoothness hyperparameters (Part 1 Table 2 & equation 5)
κ_{p0}, P_0, α	Cloud opacity profile parameters equation 1 ($m^2/\text{kg}, \text{bar}, \text{unitless}$)

^aPart I had 27 free parameters for the cloud free model. The additional parameters here are the second smoothing prior hyperparameter (see footnote(b)) and the 3-cloud opacity profile parameters.

^bThis is a new parameter not included in Part I. It adds flexibility to the inverse gamma hyper-prior distribution on γ . It could be considered a “hyper-hyper-parameter”. However, its influence was found to be negligible when comparing it to the nominal fixed value in Part I (see Table 2 in Part I).

priors, specifically the Dirichlet prior, which is suitable for compositional mixtures. Specifically we explored the the Center-Log-Transform implementation (Aitchison et al. 1986; Benneke & Seager 2012) on G1570D (from Part I) and found no meaningful difference in the posteriors, at least for the set of 7 retrievable gases included in our current model. Therefore, for continuity with Part I we choose to continue to use our “uniform-in-log” priors.

Secondly, we explore the impact of absorption cross-section resolution. Recently Grimm & Heng (2015) suggested that authors provide more specifics regarding their absorption cross-section/line list assumptions when performing radiative transfer calculations. We use the absorption cross-section data base described in Freedman et al. (2008,2014) and references there-in. Line broadening parameters are drawn from a variety of sources discussed within Freedman et al. (2008; 2014). This database contains pre-computed cross sections interpolated to a $\sim 0.01 \text{ cm}^{-1}$ resolution grid at 1060 pressure-temperature points between 75 and 4000K and 300 - 1E-6 bars. This resolution is fine enough to resolve the individual molecular lines (sampled at 1/4 the resolution of their half-widths, Freedman et al. 2008) for most species over the wavelengths we are interested in (1-2.5 μm), and for all intents and purposes can be considered “line-by-line”. Of course we do not perform our retrievals at this fine of a resolution as that would result in optical depth computations for $\sim 6 \times 10^5$ lines—too unwieldy for a retrieval. Instead we use a cross section sampling method to reduce this number. To do this we employ the method described in Sharp & Burrows (2007) where we down sample the high-resolution cross-section database to 1 cm^{-1} resolution by selecting every ~ 100 th 0.01 cm^{-1} resolution line. This has been suggested in Sharp & Burrows (2007) to be a good balance between accuracy and efficiency. Figure 2 shows a model spectrum convolved to a typical low-resolution SpeX observation (wavelength dependent resolving power, $R \sim 80\text{-}120$) under 0.01, 0.1, and 1 cm^{-1} sampling resolutions. We find that the residuals with re-

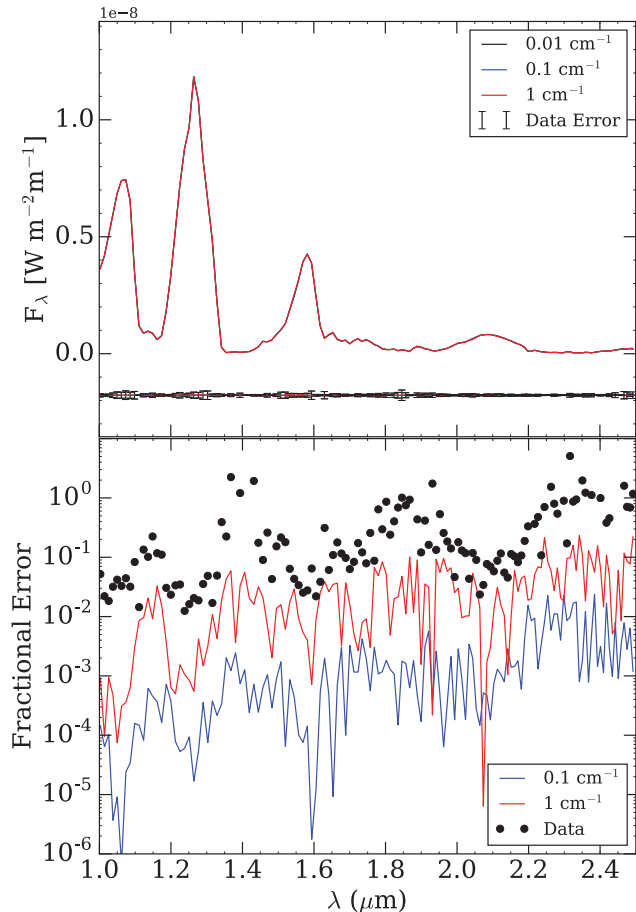


FIG. 2.— Validation of cross-section sampling method. We compare a representative model spectra generated from cross-sections sampled from 0.01, 0.1, and 1 cm^{-1} convolved and binned to the SpeX instrumental resolution ($R \sim 80\text{--}120$, depending on wavelength). The top panel directly compares the binned model spectra and the differences between the 0.1 and 1 cm^{-1} sampling and the line-by-line (0.01 cm^{-1}) to typical observational error bars. The bottom panel compares the relative (with respect to the 0.01 cm^{-1} sampling) fractional error in the 0.1 and 1 cm^{-1} sampled models to typical relative observational errors. It is readily seen that the 1 cm^{-1} sampling errors are typically well below the relative observational errors, and is therefore a sufficiently high enough sampling resolution for the SpeX instrumental resolution.

spect to the line-by-line spectra are minimal (typically an order of magnitude less relative uncertainty) relative to typical error bars, and therefore have no impact on our retrieved quantities.

Part I used a simple “slab” gray, non-scattering cloud scheme, and found its inclusion had virtually no impact on any of the other retrieved quantities for G1570D and HD3651b. Because we are exploring objects with higher effective temperatures, where clouds may become more important, we use a somewhat more complex cloud parameterization (though it turns out not to matter) to account for possible vertical variation in the cloud profile. We use similar parameterization as Burrows, Sudarsky, & Hubeny (2006) where the cloud opacity, $\kappa_c(P)$ is given by

$$\kappa_c(P) = \kappa_{P_0} \left(\frac{P}{P_0} \right)^\alpha \quad (1)$$

where P_0 is the cloud base pressure, κ_{P_0} is the spe-

cific absorption coefficient (area/mass) at the base of the cloud, and α describes shape of the cloud profile (or the cloud scale height relative to the atmospheric scale height). Given the lack of evidence for clouds in the two objects explored in Part I, and the lack of detailed cloud-diagnosing spectroscopic features beyond gray over the SpeX wavelengths, more complex parameterizations are unjustified (e.g., Morley et al. 2012).

Next we describe the sample of objects for which we perform our uniform retrieval analysis.

3. LATE T-SAMPLE

As in Part I we draw from the SpeX Prism Library (Burgasser et al. 2006a) due to the continuous spectral coverage and uniformity across hundreds of objects. We identify 11 objects within the original SpeX library² with known parallaxes that fell within the T7–T8 spectral classes (though there may be more from other sources). The normalized spectra are calibrated to flux units using the approach in Part I, but instead using the MKO H-band photometry rather than 2MASS. We briefly describe, in no particular order, the state of knowledge (of which is very heterogeneous) of each of the objects below. Table 2 summarizes the basic observational quantities required for this study and Table 3 shows the published grid-model atmosphere fits of these objects spectra and the resulting physical parameters (typically gravity and effective temperature—Derivation of physical parameters using evolutionary models, i.e., based on the object’s bolometric luminosities and assumed ages, are not included.)

HD 3651B (T7.5): This is a wide (43”; 480 AU) substellar companion to a K0V star, which also hosts a radial velocity exoplanet ($M \sin i = 0.229 \pm 0.015 M_{\text{Jup}}$; Fischer et al. 2003). The stellar parameters and activity of the primary star have been well-studied. For their analysis of the T dwarf, Liu et al. (2007) summarized the available age data for the primary based on chromospheric activity, X-ray emission, gyrochronology, and stellar-isochrone fitting, adopting the last method’s result of 3–12 Gyr from Valenti & Fischer (2005). Based on this, Liu et al. (2007) use evolutionary models and the T dwarf’s bolometric luminosity to derive $T_{\text{eff}} = 810 \pm 30$ K and $\log(g) = 5.3 \pm 0.2$. More recent isochrone-based analyses give ages of 5.13 Gyr (Casagrande et al. 2007), 6.059 Gyr (Fernandes et al. 2011), 6.9 ± 2.8 Gyr (Bonfanti et al. 2016), and 10 ± 3.5 Gyr (Ligi et al. 2016, which includes a direct stellar radius measurement from interferometry). Mamajek & Hillenbrand (2008) estimate an age of 6.4–7.7 Gyr from chromospheric activity. The primary star is well-established to have super-solar metallicity, $[\text{Fe}/\text{H}] = 0.12\text{--}0.18$, as summarized by Line et al. (2015), who also analyze the C and O abundances. This is one of the benchmark systems included in Part I.

2MASS J00501994–3322402 (T7): Radigan et al. (2014) report no variability in J band, while Wilson et al. (2014) find a 10.8% amplitude; re-analysis of the latter’s data by Radigan (2014) suggests the variability detection is spurious. Metchev et al. (2015) robustly find mid-IR [4.5] variability of 1.1% with a periodicity of 1.55 hr, among the shortest periods identified in optical/IR pho-

² <http://pono.ucsd.edu/~adam/browndwarfs/speprism/html/tdwarf.html>

TABLE 2
SUMMARY OF BASIC SAMPLE PROPERTIES

Object(SpT NIR)	H_{MKO} (mag)	d_{π} (pc)
HD 3651B ¹ (T7.5) ⁹	16.68±0.04 ⁹	11.06±0.04 ¹⁷
2MASS J00501994-3322402 ² (T7) ¹⁰	16.04±0.10 ¹¹	10.57±0.27 ¹³
2MASSI J0415195-093506 ³ (T8) ¹⁰	15.67±0.01 ¹²	5.71±0.06 ¹³
2MASSI J0727182+171001 ³ (T7) ¹⁰	15.67±0.03 ¹²	8.89±0.07 ¹³
2MASS J07290002-3954043(T8 pec) ⁴	16.05±0.18 ¹³	7.92±0.52 ¹⁸
2MASS J09393548-2448279 ² (T8) ¹⁰	15.96±0.09 ¹⁴	5.34±0.13 ¹⁹
2MASS J11145133-2618235(T7.5) ²	15.82±0.05 ¹¹	5.58±0.04 ¹³
2MASSI J1217110-031113 ⁵ (T7.5) ¹⁰	15.98±0.03 ¹⁵	11.01±0.27 ²⁰
ULAS J141623.94+134836.3 ⁶ (T7.5) ^{7,21}	17.58±0.03 ⁶	9.12±0.11 ¹³
Gliese 570D ⁸ (T7.5) ¹⁰	15.28±0.05 ¹⁶	5.84±0.03 ¹⁷
2MASSI J1553022+153236AB ³ (T7) ¹⁰	15.76±0.03 ¹²	13.32±0.11 ¹³

REFERENCES. — 1 = Mugrauer et al. (2006), 2 = Tinney et al. (2005), 3 = Burgasser et al. (2002), 4 = Looper et al. (2007), 5 = Burgasser et al. (1999), 6 = Burningham et al. (2010), 7 = Scholz (2010), 8 = Burgasser et al. (2000), 9 = Luhman et al. (2007), 10 = Burgasser et al. (2006b), 11 = Leggett et al. (2010), 12 = Knapp et al. (2004), 13 = Dupuy & Liu (2012), 14 = Leggett et al. (2009), 15 = Leggett et al. (2002), 16 = Leggett et al. (2010), 17 = van Leeuwen (2007), 18 = Faherty et al. (2012), 19 = Burgasser et al. (2008), 20 = Tinney et al. (2003), 21 = Burgasser et al. (2010b)

tometry of ultracool dwarfs. Among objects with mid-IR variability, 2MASS J0050–33 is unique in that it is only variable at [4.5] and not at [3.6].

2MASSI J0415195–093506 (T8): This well-studied object is the T8 spectral standard for the Burgasser et al. (2006b) near-IR classification scheme. From near-IR and mid-IR data, Saumon et al. (2007) inferred a likely super-solar metallicity ($[Fe/H] = 0.0-0.3$). Based on IR colors and magnitudes, Leggett et al. (2010) use models to infer that this object is slightly cooler and probably more metal-rich than Gl 570D, in agreement with the Saumon et al. (2007) spectroscopic analysis. Yamamura et al. (2010) analyze 2.5–5.0 μm *AKARI* spectra and find the non-equilibrium presence of CO and CO₂ bands likely due to significant vertical mixing, in accord with the low abundance of NH₃ in this object’s mid-IR spectrum (Saumon et al. 2006).

2MASSI J0727182+171001 (T7): This object is the T7 spectral standard for the Burgasser et al. (2006b) near-IR classification scheme. Based on a semi-empirical analysis of the near-IR spectrum using model atmospheres from the Tucson group (e.g. Burrows et al. 2006), Burgasser et al. (2006a) infer a solar metallicity for the object.

2MASS J07290002–3954043 (T8 pec): Looper et al. (2007) suggest this object may be old, as its anomalously brighter *Y*-band and fainter *K*-band peaks are suggestive of suggestive of slightly low-metallicity and/or high gravity.

2MASS J09393548–2448279 (T8): This object’s near-IR spectrum and luminosity are consistent with other objects of the same spectral class, but its mid-IR spectrum and unusually bright mid-IR flux point to a cooler object. Burgasser et al. (2006a) suggest high surface gravity and slightly subsolar metallicities given its anomalous (broad) *Y*-band and (faint) *K*-band peaks compared to objects of comparable spectral type. Leggett et al. (2007a) reach the same conclusion, and also estimate $[M/H] \approx -0.3$ from fitting the near-IR spectrum. Similarly, Leggett et al. (2009) compare the IR colors with models and find a higher gravity and/or lower metallicity than other late-T dwarfs.

Fitting the absolutely flux-calibrated near-IR and mid-IR data with model atmospheres, Burgasser et al. (2008) suggest the source is a low-metallicity ($[M/H] \approx -0.3$)

unresolved equal-mass binary, based on the unrealistically large fitted radius. Analyzing the same data, Leggett et al. (2009) also favor a binary solution, either a pair of similar 600 K dwarfs (whose temperatures would then be in discord with the near-IR type of T8) or a dissimilar pair of 700 K and 500 K dwarfs. In either binary case, Leggett et al. infer slightly sub-solar metallicity ($[M/H] \approx -0.3-0.0$). The source is unresolved in near-IR adaptive optics imaging down to 0.07'' resolution (M. Liu, priv. comm.).

Khandrika et al. (2013) report a marginal detection of *K*-band variability with large (0.3 mag) amplitude and indeterminate period. However, Radigan et al. (2014) do not find any *J*-band variability down to ≈ 0.02 mag, nor do Wilson et al. (2014) report any *J*-band variability.

2MASS J11145133–2618235 (T7.5): Like 2MASS J0939–24, Burgasser et al. (2006a) suggest high surface gravity and slightly subsolar metallicities for this object based on its anomalously broad *Y*-band and faint *K*-band peaks. Leggett et al. (2007a) agree with this assessment and also estimate $[M/H] \approx -0.3$ from fitting the near-IR spectrum.

2MASSI J1217110–031113 (T7.5): Burgasser et al. (2003) report this has a faint 0.21'' (2.3 AU) companion in their *HST* optical imaging, but Burgasser et al. (2006c) conclude this was in fact an uncorrected cosmic ray, based on a non-detection in their followup *HST* near-IR imaging. However, given the 4-year gap between the optical and NIR imaging, another possibility is that orbital motion moved the companion too close to the primary to be observed in the followup epoch. Assuming a ratio of 1.08 between the semi-major axis and projected separation for the moderate-discovery bias case of Dupuy & Liu (2011), the estimated orbital period would be 14–23 yr for a total system mass of 30–80 M_{Jup} , so significant orbital period over 4 years is plausible. The *H*-band absolute magnitude (15.77 mag) is somewhat brighter than typical for T7.5 objects (from Dupuy & Liu 2012: $M_H = 16.3$ mag using polynomial fit, 16.4 mag using averages of all T7.5’s), though within the RMS of these averages (≈ 0.5 mag). Thus, binarity remains a possibility.

Burgasser et al. (2006a) note the brighter *K*-band peak suggests reduced surface gravity compared to other late-T dwarfs, and their spectral analysis infers solar metal-

licity. Saumon et al. (2007) analysis of the near-IR spectrum indicates enhanced metallicity, with $[\text{Fe}/\text{H}]$ close to +0.3, corroborated by the $H - [4.5]$ color analysis of Leggett et al. (2010). The Saumon et al. (2007) *Spitzer* mid-IR spectrum is not good enough to constrain the NH_3 abundance and thus the degree of chemical disequilibrium, though the latter is suggested by the relatively faint IRAC [4.5] absolute magnitude in comparison to the models.

Leggett et al. (2007b) note this object’s mid-IR colors (based on L' , [3.6], and [4.5]) make it an outlier, not readily explained by gravity, metallicity, or binarity effects. These data may reflect non-equilibrium effects, though the Saumon et al. (2007) modeling does not really match the data, with possible K_{zz} values spanning an uncommonly large range of 10^2 to $10^6 \text{ cm}^2 \text{ s}^{-1}$.

Wilson et al. (2014) report possible J -band variability with full amplitude of $4.2 \pm 1.1\%$, while Radigan et al. (2014) report no J -band variability at the ≈ 0.03 mag level. Radigan et al. (2014) reanalyzed the strong variable sources from Wilson et al. (2014) and found many were not in fact variable, though her re-analysis did not include this object.

ULAS J141623.94+134836.3 (T7.5) This is a very peculiar object. Its very blue $J - K$ and very red $H - [4.5]$ colors suggest low metallicity, as does its unusual J -band peak shape and suppressed K -band flux (Burningham et al. 2010). Fits to the near-IR spectrum by Burgasser et al. (2010a) indicate both high surface gravity and low metallicity ($[M/H] \leq -0.3$). (Note that the spectra of Burningham et al. 2010 and Burgasser et al. 2010a significantly disagree about the measurement of the red wing of the J -band methane absorption, an unexplained anomaly.) The object is a $9''$ separation (82 AU) companion to the peculiar blue late-L dwarf SDSS J141624.08+134826.7 (Bowler et al. 2010; Schmidt et al. 2010), which also suggests low metallicity though its kinematics are characteristics of a thin-disk object.

Khandrika et al. (2013) find possible variability with a 30-min timescale and $\sim 11\%$ amplitude, and Radigan et al. (2014) find possible variability with $\approx 1\%$ amplitude.

2MASS J1553022+153236AB (T7) This is a $0.349''$ binary resolved with HST imagery and presumed to be a nearly equal mass T7/6.5 pair, with $\Delta F110W = 0.30$ mag, estimated component spectral types of T6.5 and T7, and an estimated mass ratio of 0.90 ± 0.02 (Burgasser et al. 2006c).

Gliese 570D (T7.5): This is an extremely well-studied object, given its brightness and the fact that it is a member of a quadruple system that includes a M1V+M3V spectroscopic binary and a K4V primary (GL 570A). Liu et al. (2007) estimate an age of 1–5 Gyr based on the available age data at the time, with more recent estimates of 1.36 Gyr from stellar activity (Vican 2012), $6.7^{+4.8}_{-4.7}$ Gyr from stellar isochrones (Casagrande et al. 2011), and 3.7 ± 0.6 Gyr from gyrochronology (Barnes 2007). Saumon et al. (2006) averaged metallicity data from the recent literature to give $[\text{Fe}/\text{H}] = 0.09 \pm 0.04$, with more recent determinations of 0.31 from Casagrande et al. (2011) and -0.05 ± 0.17 from Line et al. (2015). This is the other benchmark object explored in Part I.

4. RESULTS

Here we present the retrieval results on the spectra of 11 objects (Figure 3). The relevant retrieved and subsequently derived quantities are summarized via marginalized posterior distributions (histograms, Figure 4). The retrieved temperature profiles are summarized in Figure 5. We then present the molecular abundance results, their chemical plausibility, derived elemental abundances, and resulting diagnostic trends, implications for cloud formation, and finally comment on the retrieved evolutionary related parameters (gravity, effective temperature, and radius).

4.1. Thermal Structures

Understanding atmospheric energy balance requires knowledge of the temperature-pressure profiles (TP-profile). The TP-profile of a sub-stellar atmosphere is largely governed by the opacity structure and internal heat flux, which is in turn dictated by the mass and age (e.g., Allard et al. 1996; Burrows 2001; Saumon & Marley 2008). The two dominant energy transport mechanisms are radiation and convection. Radiative energy transport tries to eliminate any vertical radiative flux divergence. Thermal structures that meet this criterion are said to be in radiative-equilibrium. At deep enough layers, where the mean opacities are large, radiative energy transport is no longer effective at carrying the heat flux. At this point, convective energy transport dominates. The location of this radiative convective boundary is predicted to occur at pressures deeper than ~ 50 bars, or at atmospheric temperatures of $\sim 1500\text{K}$, for late T-dwarfs (Burrows et al. 2006). Additional heating due enhanced opacity from cloud particulates can sometimes result in multiple convection zones separated by a radiative zone (Burrows et al. 2006).

Other non-traditional sources of heating/cooling that could impact the TP-profiles and/or their time dependence (e.g., Robinson & Marley 2014) have been hypothesized. Latent heat release due to cloud condensation can result in a shallower adiabat than predicted from pure gas phase chemistry alone (Tan & Showman 2016), though the latent heat of typical L-T dwarf clouds are not particularly large (say, compared with water or ammonia, which are important in the solar system gas-giant atmospheres). Double diffusive convection resulting from vertical composition gradients can also result in shallower TP-profiles in the mid to deep atmospheres (Tremblin et al. 2015). Chromospheric heating can cause a more isothermal behavior in the upper ($P < \sim 1\text{bar}$) atmospheres (Sorahana et al. 2014). Additional dynamical effects like gravity wave breaking and horizontal dynamics can also cause perturbations to the TP-profile beyond the traditional assumption of 1D-radiative convective equilibrium. Determining TP-profiles over a wide range of altitudes/pressures and comparing these derived profiles to radiative-convective equilibrium profiles allows us to diagnose additional atmospheric energetic processes.

Figure 5 shows the TP-profiles for the 11 T-dwarfs in our sample. As in Part I, we summarize the TP-profiles with a median, 68%- and 95%-confidence intervals. We also show a nominal (median retrieved effective temperature and gravity) pre-computed grid model (Saumon & Marley 2008). Thermal emission contribution functions are shown to indicate where in the atmosphere we are sensing—the photosphere, typically between $\sim 50 - 0.3$

TABLE 3
SUMMARY OF SPECTROSCOPICALLY DERIVED PHYSICAL PARAMETERS FROM THE LITERATURE COMPARED WITH OUR WORK.

Object	$\lambda\lambda$ (μm)	T_{eff} (K)	$\log(g)$ (cgs)	$[M/H]$ (dex)	$\log(C/O)^a$	$\log K_{zz}$ ($\text{cm}^2 \text{s}^{-1}$)	R (R_J)	Ref
HD 3651B	1.0–2.1	790 ± 30	5.0 ± 0.3	... ^b	1
	0.7–2.5	820 – 830	5.4 – 5.5	≈ 0.2	2
2MASS J00501994–3322402	1.15–2.25	800 – 850	4.5 – 4.8	0.996 – 1.06	16
	1–2.5	719^{+19}_{-25}	$5.12^{+0.1}_{-0.2}$	$0.08^{+0.05}_{-0.06}$	$-0.05^{+0.09}_{-0.09}$...	$1.10^{+0.1}_{-0.07}$	This Work
2MASS J0415195–093506	1.0–2.1	960 – 1000	4.8 – 5.0	0	3
	1–2.5	815^{+20}_{-27}	$5.09^{+0.1}_{-0.2}$	$-0.06^{+0.05}_{-0.06}$	$0.06^{+0.09}_{-0.1}$...	$1.12^{+0.12}_{-0.09}$	This Work
2MASS J0727182+171001	1.0–2.1	740 – 760	4.9 – 5.0	0	3
	0.7–14.5	725 – 775	5.0 – 5.4	0.0 – 0.3	...	4	...	4
	1.147–1.347	947 ± 79	4.3 ± 0.7	5
	0.8–2.4	900, 1000	5.0	6
	2.5–5.0	800	4.5	1.14	7
	2.5–5.0	900	4.5	0.66	8
	1.0–5.0	700	4.5	9
	1.15–2.25	600 – 800	4.0 – 5.5	0.89 – 1.33	16
	1–2.5	680^{+13}_{-18}	$5.04^{+0.2}_{-0.2}$	$0.05^{+0.05}_{-0.07}$	$-0.01^{+0.08}_{-0.1}$...	$1.06^{+0.05}_{-0.06}$	This Work
	1.0–2.1	900 – 940	4.8 – 5.0	0	3
2MASS J07290002–3954043	0.8–2.4	1000, 1200	5.0	6
	1–2.5	807^{+17}_{-19}	$5.13^{+0.1}_{-0.1}$	$0.0^{+0.04}_{-0.04}$	$-0.09^{+0.07}_{-0.07}$...	$1.12^{+0.07}_{-0.06}$	This Work
2MASS J07290002–3954043	1.0–2.1	740 – 780	5.1	10
	1–2.5	737^{+21}_{-25}	$5.29^{+0.1}_{-0.1}$	$-0.02^{+0.05}_{-0.06}$	$-0.20^{+0.09}_{-0.1}$...	$0.95^{+0.12}_{-0.10}$	This Work
2MASS J09393548–2448279	1.0–2.1	$\lesssim 700$	3
	0.7–2.5	725 – 775	5.3 – 5.4	–0.3	2
	0.7–14.5	600	4.5	–0.3	...	4	1.26	11
	0.7–14.5	600	5.0	–0.3 – 0.0	0.88	12 ^c
	0.7–14.5	700	5.0 – 5.3	–0.3 – 0.0	0.78 – 0.88	12 (comp A) ^d
	0.7–14.5	500	5.0	–0.3 – 0.0	0.88	12 (comp B) ^e
	1–2.5	611^{+17}_{-24}	$4.88^{+0.2}_{-0.4}$	$-0.24^{+0.07}_{-0.08}$	$-0.16^{+0.13}_{-0.16}$...	$1.22^{+0.1}_{-0.09}$	This Work
	1.0–2.1	$\lesssim 700$	3
2MASS J11145133–2618235	0.7–2.5	725 – 775	5.0 – 5.3	–0.3	2
	1–2.5	678^{+22}_{-22}	$5.13^{+0.2}_{-0.3}$	$-0.06^{+0.08}_{-0.08}$	$-0.31^{+0.14}_{-0.14}$...	$0.91^{+0.09}_{-0.08}$	This Work
2MASS J1217110–031113	1.0–2.1	860 – 880	4.7 – 4.9	0	3
	0.7–14.5	850 – 950	4.8 – 5.4	~ 0.3	...	2 – 6	...	4
	1.147–1.347	922 ± 103	4.8 ± 0.7	5
ULAS J141623.94+134836.3	1–2.5	726^{+22}_{-25}	$4.74^{+0.1}_{-0.2}$	$-0.12^{+0.06}_{-0.07}$	$0.04^{+0.09}_{-0.11}$...	$1.57^{+0.11}_{-0.22}$	This Work
	0.9–2.4	650 ± 60	5.2 ± 0.4	≤ -0.3	...	4	...	13
2MASS J1553022+153236AB	1–2.5	605^{+29}_{-35}	$4.93^{+0.4}_{-0.4}$	$-0.35^{+0.10}_{-0.11}$	$-0.35^{+0.20}_{-0.19}$...	$0.8^{+0.07}_{-0.06}$	This Work
	1.147–1.347	941 ± 138	4.6 ± 0.6	5 ^f
Gliese 570D	1–2.5	803^{+16}_{-27}	$4.80^{+0.1}_{-0.2}$	$-0.19^{+0.04}_{-0.06}$	$-0.11^{+0.09}_{-0.09}$...	$1.59^{+0.14}_{-0.09}$	This Work
	1.0–2.1	780 – 820	5.1	0	3
	0.7–14.5	800 – 820	5.1 – 5.2	0	...	6.2 ± 0.7	...	14, 15
	1.147–1.347	948 ± 53	4.5 ± 0.5	5
	0.8–2.4	900	5.0	6
	1.0–5.0	700	4.5	9
	1.15–2.25	800 – 900	4.5 – 5.0	0.903 – 1.06	16
1–2.5	715^{+20}_{-22}	$4.80^{+0.3}_{-0.3}$	$-0.15^{+0.07}_{-0.09}$	$-0.10^{+0.13}_{-0.15}$...	$1.14^{+0.1}_{-0.09}$	This Work	

REFERENCES. — 1 = Burgasser (2007), 2 = Leggett et al. (2007a), 3 = Burgasser et al. (2006a), 4 = Saumon et al. (2007), 5 = Del Burgo et al. (2009), 6 = Testi (2009), 7 = Yamamura et al. (2010), 8 = Tsuji et al. (2011), 9 = Sorahana & Yamamura (2012), 10 =Looper et al. (2007), 11=Burgasser et al. (2008), 12 = Leggett et al. (2010), 13 = Burgasser et al. (2010a), 14 = Saumon et al. (2006), 15 = Geballe et al. (2009) 16 = Liu et al. (2011)

^aThis is *not* relative to solar, but absolute. Solar C/O (0.55) would be a $\log(C/O) = -0.26$ in this column.

^bSpectral fits assumed $[M/H] = 0.12 \pm 0.04$, as derived from the primary star HD 3651A.

^cAssumes system is an unresolved equal-mass binary.

^dAssumes system is an unresolved unequal-mass binary.

^eAssumes system is an unresolved unequal-mass binary.

^fFit does not account for binarity.

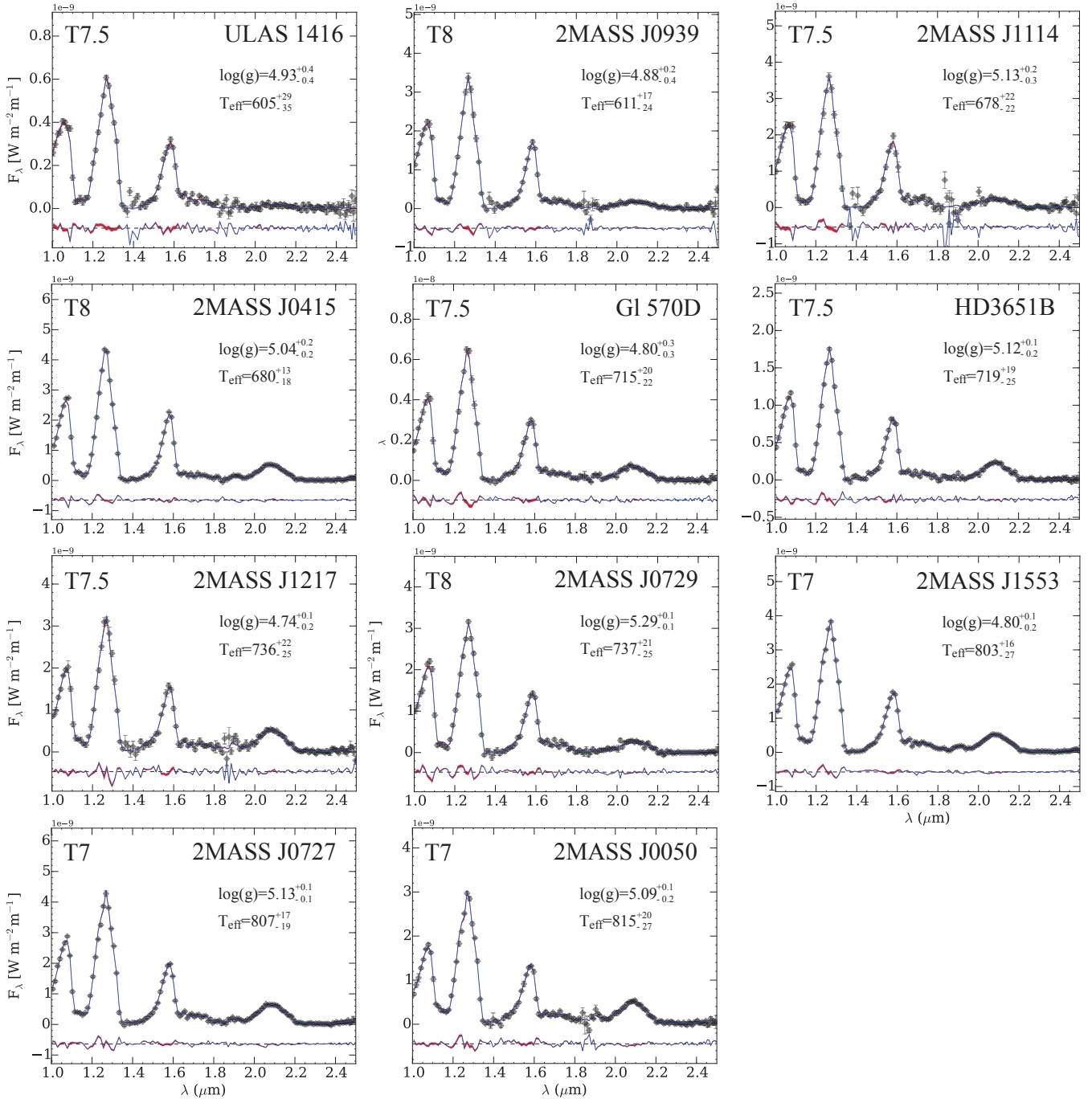


FIG. 3.— Summary of SPeX data used in this investigation along with their fits. The data are indicated with the gray diamonds with error bars. The retrieval fits are summarized with a median (blue), 1- and 2-sigma confidence intervals (red, pink respectively) for spectra computed from 1000 random parameter vectors drawn from the posterior. Note the small spread. Residuals are shown below the spectra to illustrate the good quality of the fits. The near-infrared spectral type is given in the upper left hand corner and the object name in the upper right. The retrieved $\log g$ and derived effective temperature and their uncertainties are also given.

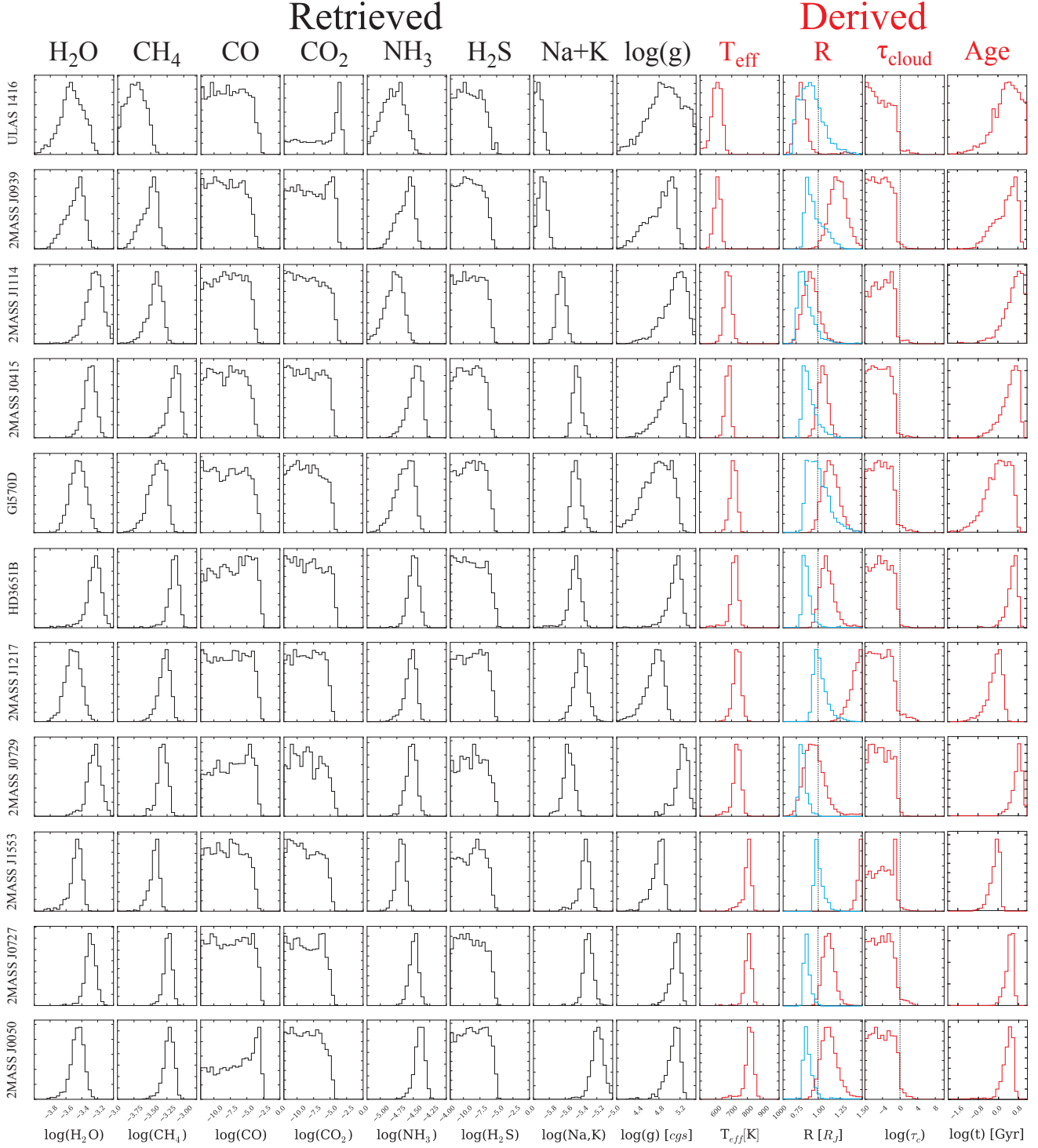


FIG. 4.— Histograms summarizing the marginalized posterior distributions of the relevant retrieved and subsequently derived quantities. We show only the retrieved molecular abundances and gravity. All other parameters are either nuisance parameters (e.g., TP smoothing parameters, wavelength shifts, error bar inflation parameter) or summarized elsewhere (e.g., TP-profile). The derived quantities (shown in red) are not directly retrieved from the data but are rather inferred/derived from quantities that are retrieved. The effective temperature (T_{eff}) is derived by equating Boltzmann’s law to the bolometric fluxes (1-20 microns) derived from 5000 spectra drawn from the posterior. The photometric radius (R) is obtained from the $(R/D)^2$ scaling parameter given the distances (D) and photometric calibration uncertainties. We also show for comparison (in blue) the evolutionary derived radius from the retrieved effective temperature and gravity using the relations in Burrows et al. (2001) (see §4.4 for details). The dotted vertical lines represent 1 Jupiter radius. The cloud column optical depth (τ_{cloud}) is derived by integrating the cloud opacity profile (obtained from the retrieved quantities in equation 1) over the photospheres (see Figure 5). The dotted vertical lines denote an optical depth of unity. Finally, the last column shows the evolutionary derived age from the effective temperature and gravity, again using the relations in Burrows et al. (2001).

bar. The Y-, and J-band peaks probe the deepest levels, while the high opacity regions between these bands probe the lowest pressure levels (highest altitudes). The TP-profiles within the photosphere are considered the most robust. Typical 1-sigma photospheric temperature uncertainties are ~ 30 -100 K. TP-profile information outside of those regions ($P > 50$ bar and $P < 0.3$ bar) are largely driven by the TP-profile parameterization (via the smoothing prior described in detail in Part I) and should not be too heavily interpreted. Finally, we show the equilibrium condensation curves for KCl, Na₂S, and MgSiO₃.

In general, as we found for the two objects explored in Part I, the retrieved TP-profiles and predicted radiative-convective equilibrium grid models agree quite well over the photosphere. Deviations begin to occur outside of the photosphere. In Part I we suggested that the shallower TP-profile gradient below the ~ 50 bar level maybe indicative of the double-diffusive convection suggested by Tremblin et al. (2015). However, there is very little contribution to the overall emission at these deeper levels due to the increasing opacity of the collision induced molecular hydrogen along with the alkali metal and water opacities at the J- and Y-band peaks. Above the photosphere ($P < 0.3$ bar), we typically find that the TP-profiles become more isothermal than predicted from radiative-convective equilibrium, possibly hinting at some sort of additional heating, but again, temperature constraints are unreliable in this region.

Late T-dwarfs (and Y-dwarfs) offer the best chances of learning about the TP-profiles of brown dwarfs because of the large spectral dynamic range sculpted by strong water vapor absorption and predominately cloud free atmospheres. This high spectral dynamic range provides leverage on the TP-profile over a wide range of photospheric pressures. However, as seen here, it is difficult to push towards deeper pressures due to the increasing significance of collision induced opacities. Higher resolution spectra near the water band-heads (between the Y-J-H bands) or longer wavelengths with higher opacity could allow us to probe *lower* pressures (higher altitudes) than probed here, permitting more precise upper atmosphere temperature constraints. Hotter objects, mid T-s and beyond, will present a challenge as their photospheres narrow due to the presence of clouds, preventing us from accessing the deeper atmospheric levels. Any temperature profile information below where the cloud opacities become large will have to come from extrapolation via parameterizations or assumed from physically motivated models. Regardless, assumptions will have to be made and these assumptions will have to be tested.

4.2. Composition & Chemistry

We show, for the first time, the molecular abundances derived for an ensemble of T-dwarfs. Molecular abundance determinations are diagnostic of the atmospheric chemical processes as well as the underlying elemental abundances. We present the retrieved uniform-with-altitude molecular abundances for 7 gases: H₂O, CH₄, CO, CO₂, NH₃, H₂S, Na+K, where Na+K represents the combination of sodium and potassium, where their

ratio is assumed to be solar³. The first 7 columns of Figure 6 show the marginalized gas posterior distributions for the 11 objects, sorted in effective temperature (low - high). As in Part I, we find that H₂O, CH₄, NH₃, and the alkalis are the only species with bounded constraints. We can derive only upper limits for the other species (CO, CO₂, H₂S), consistent with a non-detection of these gases (e.g., see the Bayes Factor analysis in Part 1). This is unsurprising given their low abundances predicted from thermochemical equilibrium (Lodders et al. 2002).

4.2.1. Comparison to Equilibrium Chemistry Predictions

Because we are retrieving each gas phase absorber individually, it is possible to obtain chemically implausible combinations (e.g., Heng & Lyons 2016; Stevenson et al. 2014). It is therefore prudent to check the plausibility of our results against a chemical model. For simplicity, we compare our results to predictions from a thermochemical model (Chemical Equilibrium with Applications Code 2, Gordon & McBride 1996, see Part I for implementation details and relevant references) in Figure 6. Briefly, the model computes the thermochemical equilibrium molecular ratios at a given P-T pair and set of elemental abundances (Lodders & Fegley 2002). The model accounts for both gas phase and condensed phase species in local thermochemical equilibrium, but does not take into account the rain-out paradigm whereby elemental species are depleted due to their sequestration into condensates that form large droplets and “rain” out into the deeper unobservable atmosphere (e.g., Fegley & Lodders 1994; Marley & Robinson 2015). We do accommodate for the influence of main rain out process (enstatite and forsterite condensation, Fegley & Lodders 1994) on the elemental abundances (and subsequent equilibrium molecular abundances) by manually removing 3.28 oxygen atoms per silicon atom (Sharp & Burrows 1999).

As in Part I, we compute the equilibrium molecular abundances along the median of the retrieved TP-profiles for each object (from Figure 4). We compare the retrieved molecular abundances for only the well constrained species (shaded regions in Figure 6) to the equilibrium composition computed with solar elemental ratios (solid curves in Figure 6). In general we find that the retrieved mixing ratios qualitatively agree with what is expected from thermochemical equilibrium at these temperatures: CH₄ and H₂O are the most abundant species followed by NH₃ and then the alkalis. We emphasize that both the retrieved and thermochemically calculated mixing ratios are really only relevant over the photosphere (~ 30 - 0.3 bar, Figure 4). Upon more careful inspection we find some inconsistencies between the thermochemical predictions at solar composition and the retrieved mixing ratios. We then adjust the metallicity ($[\text{Fe}/\text{H}]$)⁴ by rescaling all elements heavier than H and He and the carbon-to-oxygen ratio (C/O) to by-hand “fit” the thermochemical model (dashed curves in Figure 6 corresponding to the inset values) to the retrieved mixing

³ We do this because the low-res SpeX data is really only sensitive to the red pressure broadened wings of these species, and to reduce the overall number of retrieved gases. Certainly the sodium-to-potassium ratio need not be solar, a quantity worth deriving from higher resolution spectra.

⁴ In this context we mean the sum of all elements other than H and He.

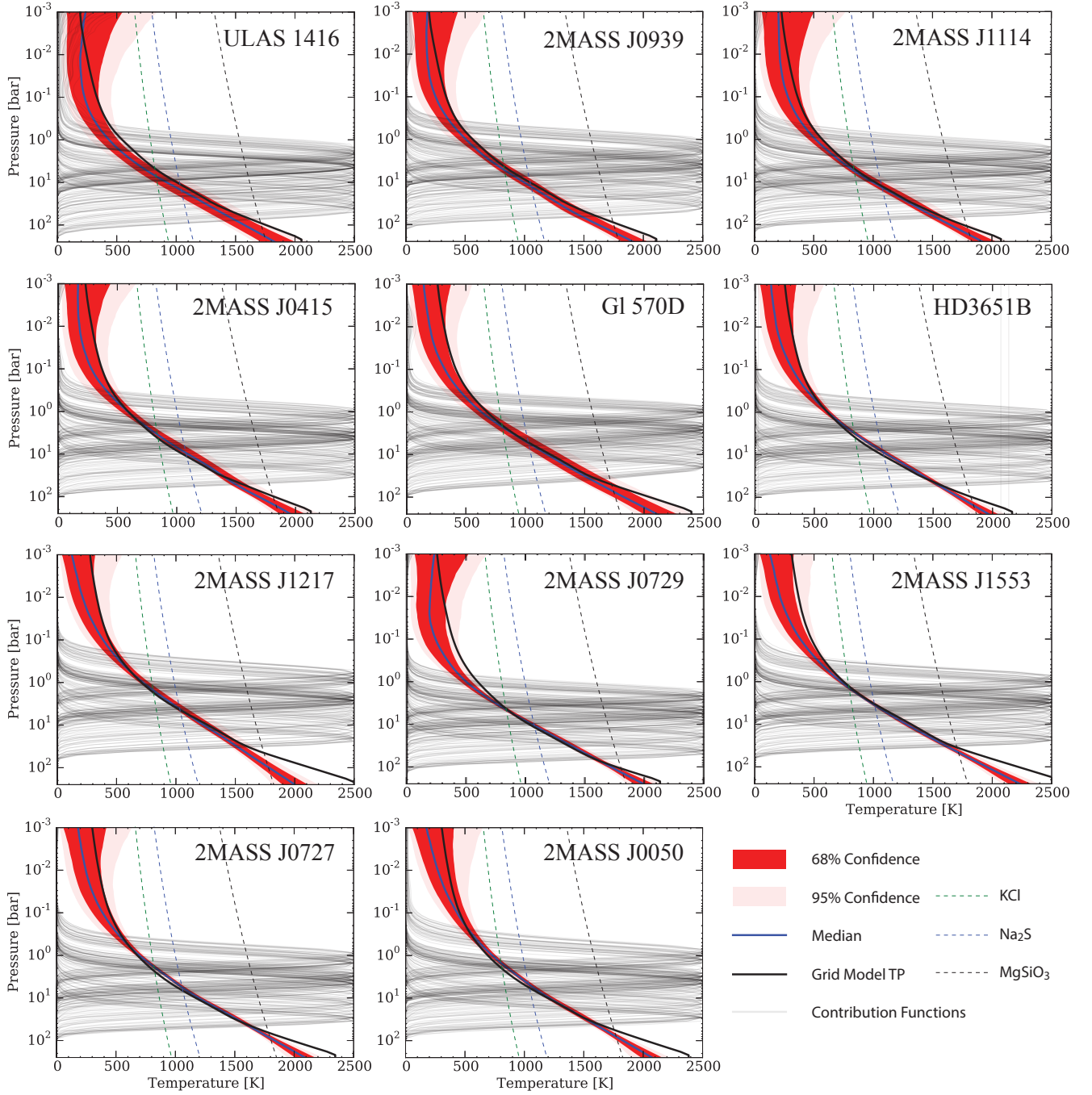


FIG. 5.— Retrieved temperature profiles. The median, 68%, and 95% confidence intervals are shown in blue, red, and pink, respectively. The light gray curves are the thermal emission contribution functions for each SPeX wavelength for a representative fit. These represent the location of the photosphere. The black curve is a TP-profile from a self-consistent grid model (Saumon & Marley 2008) corresponding to the median of the retrieved $\log(g)$ and effective temperature. Finally, the dashed curves are the equilibrium condensation curves for KCl, Na_2S , and MgSiO_3 from Morley et al. (2012) (and references therein), adjusted to the appropriate metallicity. The characteristic shape of the retrieved TP-profiles is in good agreement with self-consistent radiative-convective equilibrium predictions over the photosphere. The divergence below the photosphere is largely due to the lack of spectral information probing the deeper levels.

ratios, exactly as was done in Part I. This is by no means a rigorous fit (see §4.3.1 for a more quantitative analysis), but is meant to show that we can obtain consistency between the thermochemical prediction and the retrieved mixing ratios by adjusting these two quantities, suggesting that we have retrieved *chemically plausible* molecular abundance combinations.

We do find some preliminary, though not robust, evidence of disequilibrium ammonia chemistry (as discussed in Saumon et al. 2006; Cushing et al. 2008; Stephens et al. 2009 with respect to mid infrared data). For most objects the thermochemically computed value of ammonia over the photospheric pressures probed by SpeX is lower than the retrieved values. However, the thermochemical predictions at the artificial base of the atmosphere are consistent with the retrieved values, suggesting a deep quench level ($\sim >100$ bars) could be possible in explaining the ammonia mixing ratios. Finally, we find some inconsistencies in between predicted and retrieved alkali abundances. This could be due to the difficulties in properly modeling the far pressure broadened wings of the alkali lines (Allard et al. 2009) and/or the details of condensate rainout chemistry (of which our model does not account for), though it need not be that all elemental abundance ratios are solar.

In the next section we will use this thermochemical modeling approach to derive the intrinsic bulk metallicity and carbon-to-oxygen ratios for each object.

4.2.2. Retrieved Species Trends & Possible Direct Evidence of Condensate Sequence

An advantage of retrieval methods over grid models is that we can directly determine the molecular abundances rather than assume/compute them, and from trends in those abundances, infer physical/chemical processes. As an initial look, we focus on molecular abundance trends with effective temperature (Figure 7). Chemical processes (e.g., equilibrium chemistry, condensate processes) tend to depend strongly on temperature (e.g. Burrows & Sharp 1999, Lodders & Fegley 2002); we would therefore expect molecular abundances to change with temperature. Specifically, we focus on trends associated with the well constrained species, e.g. those with bounded constraints, which include H_2O , CH_4 , NH_3 , and the alkali metals. The other species (CO , CO_2 , and H_2S), while chemically interesting, simply do not have the precisions required to identify diagnostic trends.

We would predict water and methane to have little or no trend with temperature over our sample temperature range ($\sim 600\text{-}850$ K) as they are thermochemically constant (e.g., Burrows & Sharp 1999 Figure 5) and largely unaffected by disequilibrium processes (Saumon et al. 2006) at these temperatures. Unsurprisingly, we indeed do not find any statistically robust trends of water and methane with temperature, as both are consistent with the null, no-trend, hypothesis (Figure 7, top panels). Ammonia (Figure 7, bottom left), on the other hand, is thermochemically predicted to decrease by nearly an order of magnitude over this temperature range over the photospheric pressure levels (Burrows & Sharp 1999). Given the uncertainties, we should be able to identify such a trend if it existed; the lack of trend is interesting. Perhaps the lack of trend is speaking to perturbations due to disequilibrium chemistry dredging up ammonia from

these deeper layers. Depending on the degree of dispersion in the vertical mixing strength amongst these objects (can depend on internal heat flux, rotation rate, magnetic field strength, Flasar and Gierasch, 1977; Visscher et al. 2010), it is not surprising that the thermochemically predicted trend of decreasing abundance with temperature is not so clearly borne out.

A more striking trend is that of the alkali metal abundances with temperature (Figure 7, bottom right), with the null hypothesis being rejected at $>25\sigma$. Over the $\sim 600\text{-}850$ K range, the alkali metal abundance increases by nearly an order of magnitude. We attribute this trend to the condensation of salt sulfide (Na_2S) and potassium chloride (KCl) clouds (dominated by the KCl condensation as K dominates the alkali absorption nearby Y-band by a few to ~ 1 order magnitude over Na at solar Na/K ratios)⁵. The general hypothesis being, that as these objects cool, the TP-profile-condensate intersection point moves deeper into the atmosphere (as seen in Figure 5 where the dashed curves intersect the blue solid blue curve). Gas phase sodium and potassium only exist in appreciable quantities *below* the TP-profile-condensate intersection point. Therefore, as the TP-profile-condensate intersection point moves deeper into the atmosphere, the overall integrated column abundance of gas phase elemental sodium and potassium decreases over the photospheric regions. This is hypothesis is further confirmed in Figure 8. The left panel shows the pressure levels where the Na_2S and KCl condensate curves intersect the retrieved TP-profiles for each object (as can be readily determined from the TP-profiles in Figure 5), as a function of effective temperature. As expected, as cooler temperatures occur at lower pressures for hotter objects, the condensates are in turn expected to form at these lower pressures (higher altitudes). We can then map back the retrieved alkali abundance trend with the pressure level of of the TP-profile-condensate intersection. Indeed we do find a trend, thus confirming our argument that hotter objects have a greater column of gas phase alkalis, of which our ensemble analysis is sensitive to.

There have long been two ‘schools’ of how condensate chemistry should be treated in brown dwarf atmospheric models. In the pure equilibrium school condensates are considered to continue to be in chemical equilibrium with their surrounding gas, even after condensation (for example Burrows & Sharp 1999). In the second school, commonly followed in solar system chemistry (Fegley & Lodders 1994) condensed species ‘rain out’ of the atmosphere and are no longer available to react with surrounding gas at lower temperatures. In the pure equilibrium school for example gaseous Na and K react with previously condensed aluminum and silicate compounds to form feldspar minerals such as sanadine and albite (see Burrows et al. 2001 for a discussion). Meanwhile in the rain out conception the aluminum oxides and silicates rain out of the atmosphere after they condense and the feldspars do not form. Instead the gaseous Na and K form chloride salts at much lower temperatures (Lodders 1999). A number of lines of evidence (Marley

⁵ while Na is ~ 20 times more abundant than K, the absorption cross section of K is ~ 100 greater at shorter wavelength resulting in K dominating the opacity by nearly an order of magnitude

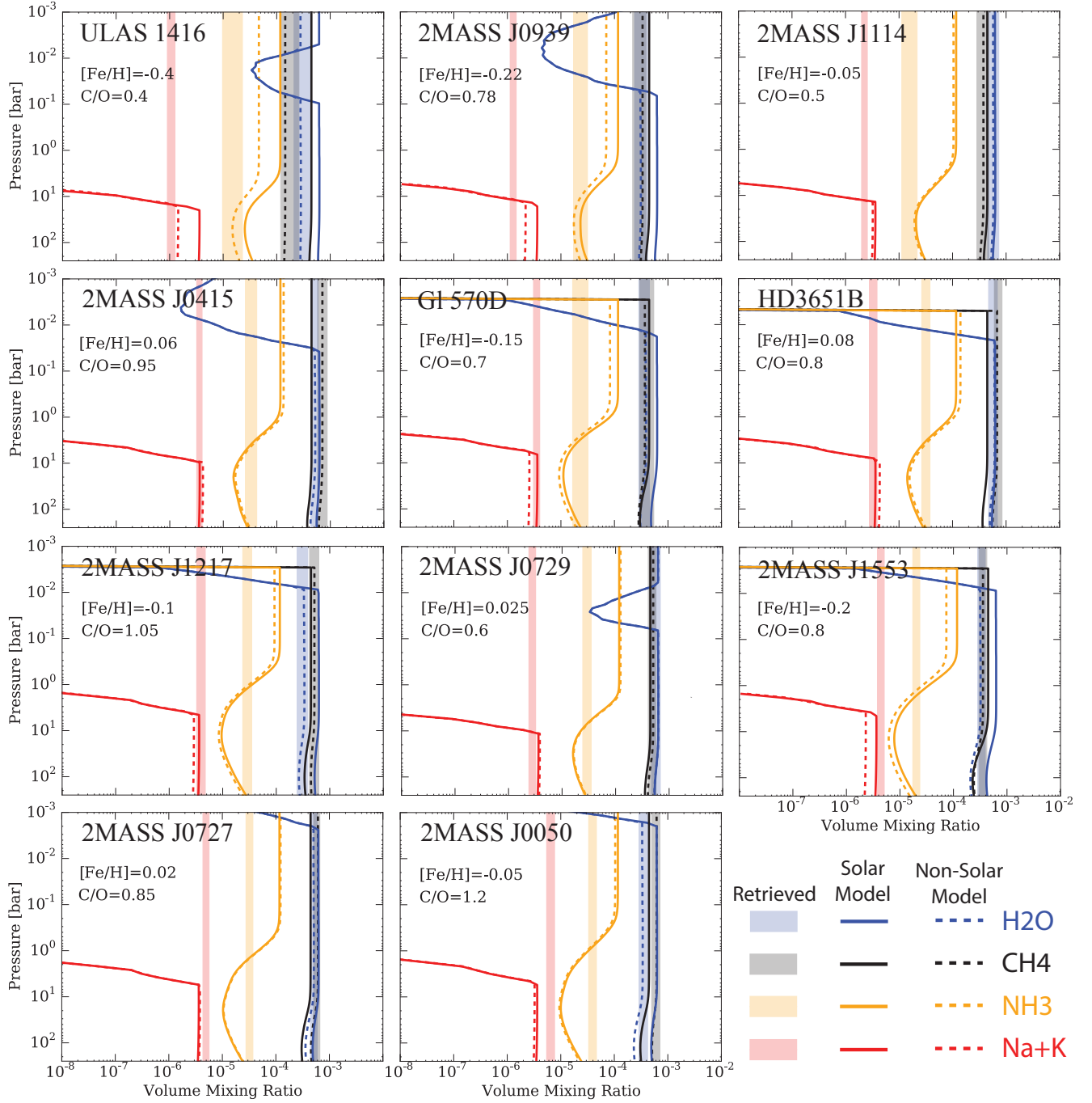


FIG. 6.— Comparison of retrieved abundances for well constrained species (Na/K, CH₄, H₂O, and NH₃) to thermochemical model predictions. The 1-sigma uniform-with-altitude mixing ratios retrieved from the data are indicated by the shaded rectangles. Thermochemical equilibrium molecular mixing ratios computed along the median TP-profile's assuming solar elemental abundances are shown as the solid curves. Finally, the dashed curves are the thermochemical equilibrium mixing ratios computed along the median TP-profiles assuming the metallicity, $[\text{Fe}/\text{H}]$, and C/O values indicated in each panel. These quantities were adjusted to achieve a "by-eye" good match to the retrieved mixing ratios over the photosphere. The metallicity here, $[\text{Fe}/\text{H}]$, is defined as the log of all species heavier than hydrogen/helium relative to hydrogen/helium, relative to that ratio for solar, e.g., $[\text{Fe}/\text{H}] = 0$, and $\text{C}/\text{O} = 0.55$ is solar where as $[\text{Fe}/\text{H}] = 1$ would be 10x the solar metal abundance. In general, the retrieved mixing ratios can be reproduced thermochemically given a proper tuning of the metallicity and C/O ratio, suggesting that the retrieved mixing ratios are thermochemically plausible. Note that we do not treat rainout here, rather pure local thermochemical equilibrium with all ~ 2000 species in the CEA/Thermobuild library (Gordon & McBride 1996). We do however, account for the depletion of oxygen due to presumed enstatite rainout which is predicted to remove 3.28 oxygen atoms per silicon atom (Burrows & Sharp 1999).

et al. 2002, Morley et al. 2012), have pointed towards rainout chemistry as being the most applicable to brown dwarf atmospheres, but conclusive evidence of Na and K depletion in the atmosphere over the expected temperature range has been somewhat lacking. Given our observed trend, and its correlation with the condensate base pressure, we have provided definitive evidence that this rain out paradigm is indeed correct.

4.3. Clouds

As demonstrated in §4.3.1 and §4.2.2, condensates are likely responsible for the depletion of oxygen and the alkali metal trend. We might anticipate the resulting clouds to impact the spectrum. As such, we have included the impact of a gray non-scattering cloud in our retrieval scheme (equation 1). To investigate the importance of clouds, from the three retrieved cloud parameters in equation 1 we can compute the column integrated optical depth histograms over the photospheres for each object, shown in the last column (τ_{cloud}) of Figure 4. The cloud optical depth histograms for each object all show a dramatic decline in probability near optical depths of unity (vertical dotted lines). This suggests that for these objects, larger cloud optical are rejected by the data indicating that optically thick clouds are not present. This is consistent with our findings in Part I where we applied Bayesian hypothesis testing to show that the inclusion of clouds for Gl570D and HD3651B was not justified given the data nor did their inclusion impact the retrieved values for any of the other parameters. We note, that for some objects there is a small trickle of probability towards higher optical depths, though not significant relative to the total integrated probability.

The lack of large cloud optical depth is in reasonable agreement with expectations for late T-dwarfs from forward modeling investigations (Lodders 1999; Lodders & Fegley 2002; Visscher et al. 2006;2010; Morley et al. 2012). Based upon the intersection of the enstatite condensation curve with the TP-profiles (Figure 5), we find that the silicate clouds largely reside below the photosphere, e.g., the gaseous opacities become optically thick at pressure levels above where the enstatite cloud should form and thus should have no impact on the emergent spectrum. This is consistent with the findings of Morley et al. (2012), where forward models of objects covering a similar temperature range suggest that the silicate clouds are largely below the photosphere except for the objects approaching $\sim 900\text{K}$. Figure 5 and the alkali metal trend suggests that Na_2S and KCl clouds should form within the photosphere. Morley et al. (2012) showed that the largely neglected cloud species Na_2S , KCl , MnS , and ZnS can form within cool dwarf atmospheres. They showed that, depending on gravity and the degree of droplet sedimentation (higher gravity and more vertically extended clouds result in higher cloud optical depths), the optical depths of Na_2S (more so than KCl) can range from negligible to a few within the $1\text{-}6\mu\text{m}$ photospheres of late T-dwarfs (their Figure 4 and 8). Our photospheric optical depth upper limits suggest that the cloud optical depths cannot be significantly greater than unity⁶. This may potentially place constraints on the vertical extent of the clouds, largely favoring more ver-

tically compact clouds (higher degree of sedimentation within their modeling framework). Continued work on determining more precise cloud optical depth upper limits, and or even bounded constraints on cloud optical depths, will be invaluable in constraining cloud physics in substellar atmospheres.

4.3.1. Metallicity & Carbon-to-Oxygen Ratio Determination

The elemental abundances of a star or substellar object are diagnostic of their formation history and evolution as well as atmospheric chemical and physical processes (Bond et al. 2010; Burrows 2001; Marley & Robinson 2015). Detailed stellar/substellar abundances are also critical to the understanding of galactic chemical evolution (Timmes et al. 1995; McWilliam 1997; Venn et al. 2004). There has been a recent push to obtain high precision stellar abundance measurements of many elements around solar type stars in order to better understand planet formation (Petigura & Marcy 2011; Teske et al. 2014; Fortney 2012). Much work has gone into determining stellar abundances, but it is by no means a solved problem as different methods and stellar parameter assumptions can result in different elemental abundance determinations (e.g., Hinkel et al. 2016).

While solar-type abundance determinations have received much attention, little work has been done in determining brown dwarf elemental abundances beyond their metallicities (e.g., Cushing et al. 2008; Stephens et al. 2009). Planets have been hypothesized (Payne & Lodato 2007), and some detected (Han et al. 2013), around brown dwarfs. Brown dwarfs will eventually provide a unique opportunity to detect/explore habitable planets via the transit method due to their favorable separation and radius ratios (Belu et al. 2013). We would therefore expect that in the not too distant future, brown dwarf elemental abundances determinations will become increasingly more important.

The challenging aspect of elemental abundance determinations in cool substellar objects (M-dwarfs included) is the presence of molecular species and condensates. Molecular species and condensates sequester what would otherwise be liberated elements available to form atomic absorption lines. Furthermore, the nature of their broad-band absorption obscures the precious continuum so often required in classic stellar elemental abundance analysis (e.g., Bean et al. 2006). Therefore, novel methods need to be employed in order to leverage the molecular absorption to obtain the intrinsic elemental abundances. Even then, molecular abundances can be readily perturbed by atmospheric processes like vertical mixing and equilibrium cloud condensation. These processes need to be taken into account when inferring elemental abundances from molecular absorption. While there has been effort to infer metallicities (Cushing et al. 2008; Stephens et al. 2009) and other properties (cloud thickness, gravity, effective temperature), many of these types of investigations of rely upon grids of pre-computed grid models over just a few parameters (for instance non-solar C/O is often not accounted for). Often times these grid

assume that the clouds are purely absorbing. It is therefore possible that there exist higher optical depth clouds, but that have non-zero single scatter albedo's (ω), which would allow for higher optical depths by a factor of $\sim(1-\omega)$

⁶ However, we do not include multiple scattering, that is, we

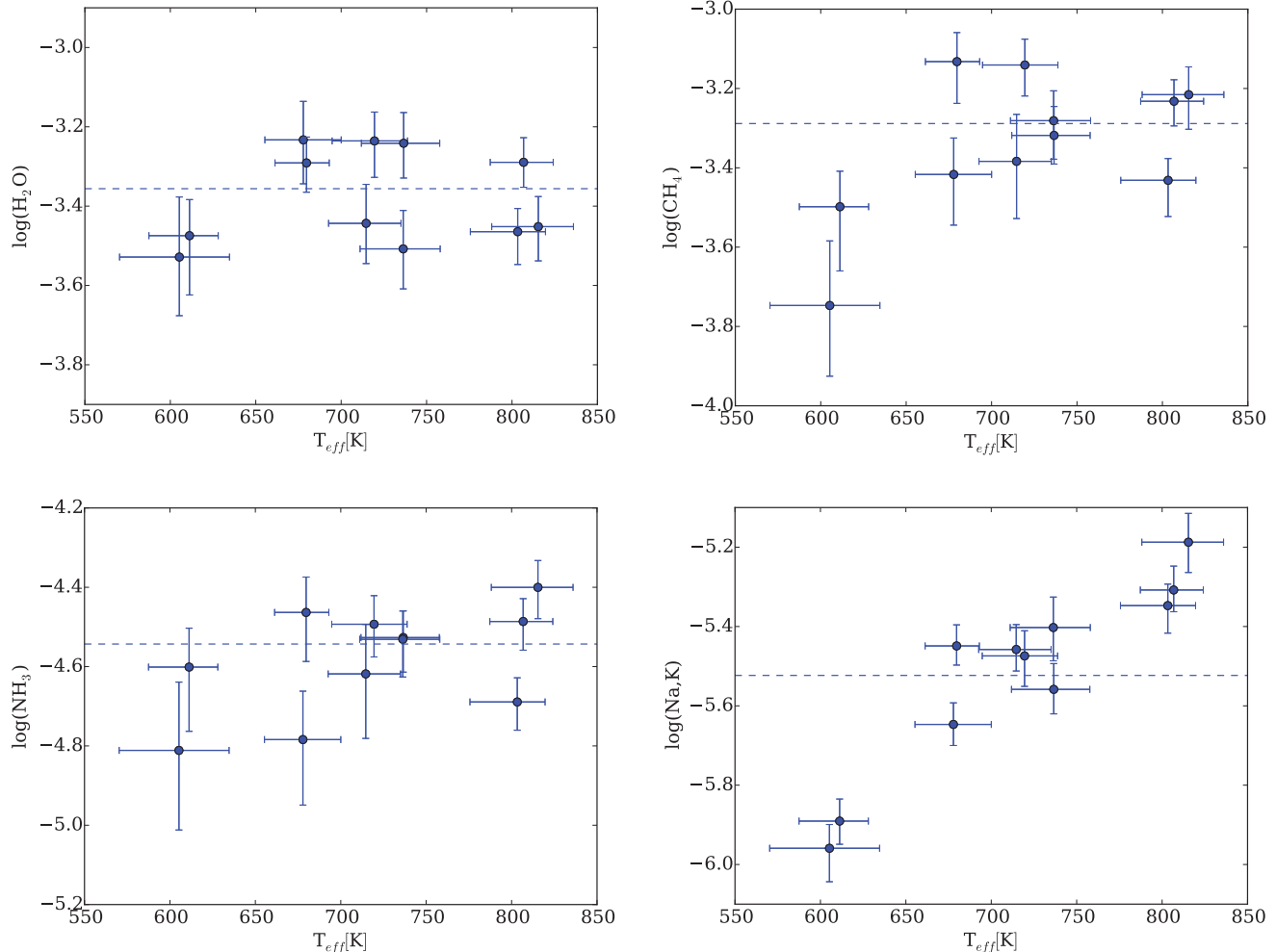


FIG. 7.— Molecular abundance trends with effective temperature for the well constrained species. The y-axis scale for each species spans 1 order of magnitude to facilitate in comparing the constraints from one species to the next. The horizontal dashed line in each panel is the abundance error weighted mean for each molecule, or equivalently, the best fit “no-trend” constant. To compute the statistical significance of any trends, we rather determine how well we can reject the null (no trend) hypothesis. We can reject the null hypothesis at 1.0, 2.9, 0.9, and 26.9 σ for water, methane, ammonia, and the alkalis, respectively. The only truly robust trend is that of the alkali metals with temperature. All other trends are reasonably consistent with a horizontal line.

models don’t adequately fit the data (e.g., Patience et al. 2012) and/or do not account for uncertainties in missing model physics as that physics is a-priori prescribed. Our retrieval methodology relaxes these assumptions and allows for more satisfying fits to the data. The danger, again being, the possibility for “unphysical” solutions, e.g., solutions that do not conform to reasonable chemical/physical assumptions. However, as demonstrated in §4.1 and 4.2.1 we are indeed deriving physically/chemically plausible atmospheric properties.

We proceed to derive the elemental abundances from the molecular abundances using the thermochemical model described in §4.2.1 as follows. We first parameterize elemental abundances with the C/O and metallicity. We then focus on CH_4 and H_2O as the metallicity and C/O diagnostics since their mixing ratios are not strongly influenced by chemical quenching at these temperatures (in contrast to say, NH_3 and CO). These are the molecular abundance “data” that we will fit. We execute a more rigorous (in contrast to §4.2.1) fit to the molecular abundances by applying the “chemical retrieval-on-retrieval”

method described in Line et al. (2016).

The basic method is to fit the retrieved water and methane mixing ratio posteriors with the thermochemical model with the free parameters being the C/O and metallicity using EMCEE. The exact “data” being fit here are the water and methane histograms from Figure 4. At each MCMC step a TP-profile is randomly drawn from the retrieval posterior in order to propagate the TP-profile uncertainty into the C/O-metallicity results. Given the randomly selected TP-profile, the C/O and metallicity for that MCMC step, the thermochemical abundances of methane and water are computed at a representative photospheric pressure (3 bars, and corresponding temperature at that pressure level), and evaluate their probability of occurrence from the methane and water histograms. These two probabilities are then multiplied and logged to compute the equivalent of “chi-square”. Note that we could have a-priori fit the water and methane histograms with a Gaussian ahead of time to derive a “data point” with an error bar of which we could then use the chi-square formula. However, the “fit

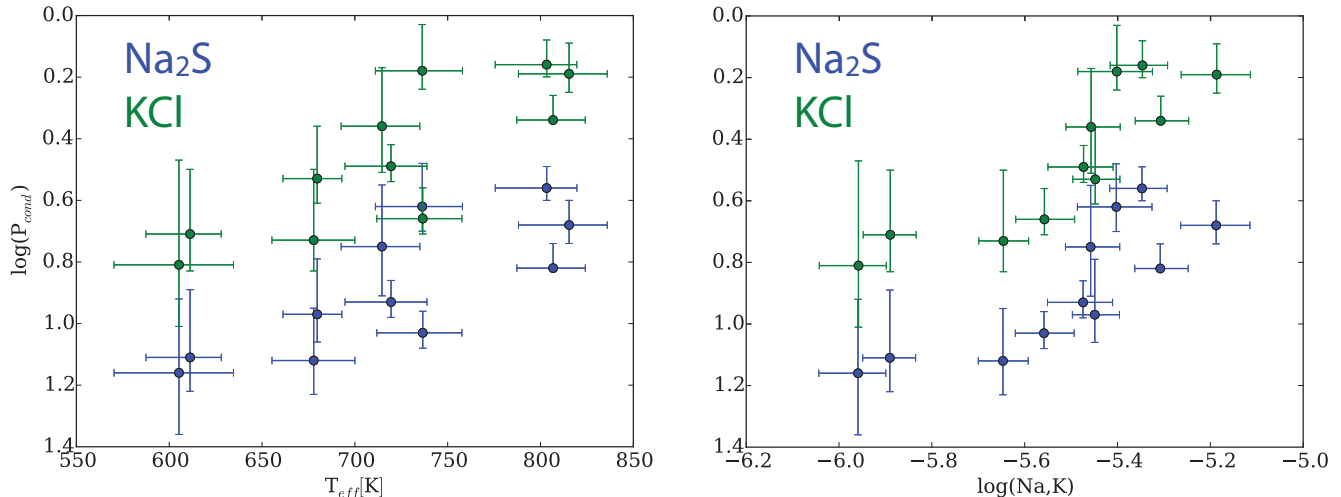


FIG. 8.— Comparison of TP-condensate intersection pressure with effective temperature (left) and alkali metal abundance (right). Hotter effective temperatures correspond to overall hotter TP-profiles (from Figure 5) causing the intersection point to move towards lower pressures (higher altitudes). As the TP-condensate intersection point moves towards lower pressures, a greater integrated column abundance of the alkali metals is allowed (dominated by the K opacity), suggesting that the alkali trend is consistent with alkali rainout.

the histogram” approach is more rigorous because it can account for any arbitrarily shaped distribution (see Line et al. 2016 for details) and is fundamentally what minimizing chi-square tries to do anyway.

We apply this procedure under two different condensate rainout assumptions. The first assumes no rainout, e.g., pure equilibrium. All condensates remain in the atmospheric layer at which they formed. The second is the silicate⁷ rainout paradigm as it affects oxygen whereby we remove 3.28 oxygen atoms per silicon atom (as was done in §4.2.1)⁸. Silicate condensation, and subsequent rainout, occur below the photosphere where the TP-profiles intersect the silicate condensate curves (Figure 5 shows enstatite). Essentially, we are simplistically exploring the effect that different condensation assumptions can have on the derived elemental abundances. Recall that only photons emanating from a relatively thin slab of atmosphere are accessible by the observations. Unseen processes occurring outside of the photosphere can impact the molecular abundances that we retrieve within the photosphere. We must indirectly account for these processes.

Figure 9 summarizes the results of this analysis. We find that our sample tends to have an overall sub-solar metallicity and super-solar C/O. Given that the retrieved water abundances for all objects is greater than or equal to the methane abundance, it is unsurprising that we in turn derive a super solar C/O. We also find that the rainout assumption can have a fairly significant effect on the derived C/O and metallicity. Increasing the amount of oxygen lost because of rainout “shifts” the population towards more solar-like abundances. One could imagine that if an even more efficient mechanism for oxygen sequestration existed (e.g., hydrated mineral formation

via something like Montmorillonite) or some other unaccounted for condensation mechanism), these objects would further shift towards the solar values. We are rather confident in robustness of our methods and assumptions used to derive these quantities given the good metallicity and C/O agreement in the benchmark systems, Gl570 and HD3651 from Part I.

Next, we compare the brown dwarf metallicities and carbon-to-oxygen ratios to those of the local F-G-K stellar population in Figure 9 derived from the Hypatia catalogue (Hinkel et al. 2014). We do not intend to delve into the details of stellar abundance determinations, suffice it to say, that it is indeed no trivial task and often different datasets and methodologies can lead to inconsistent results (e.g., Hinkel et al. 2016), resulting in relatively large systematic abundance uncertainties per any given star. In general, we find that the objects in our sample tend to lie towards lower metallicities and higher carbon-to-oxygen ratios than the bulk of the stellar population. The reason for this as of now, is unknown, but we again, hypothesize that it may have to do with how efficient oxygen is sequestered into condensates, preventing us from determining the true oxygen inventory. More detailed thermochemical condensate modeling is required to identify additional sinks of oxygen.

It is also possible that the Si/O ratio need not be in solar (e.g., Hinkel et al. 2014). With higher Si abundances, more oxygen could be depleted through silicate rainout. Both $[\text{Si}/\text{Fe}]$ and $[\text{O}/\text{Fe}]$ are known to decrease within decreasing $[\text{Fe}/\text{H}]$ in the stellar population (Figure 5 & 7 in Hinkel et al. 2014) because they are α -elements (e.g., Gratton & Ortolani 1986; Marcolini et al. 2009). However, oxygen tends to decrease more than silicon with decreasing $[\text{Fe}/\text{H}]$, suggesting that lower metallicity objects should have a *greater* proportion of O relative to Si than at higher metallicities. Why the intrinsic Si/O would be preferentially higher amongst brown dwarfs is unknown.

⁷ We only account for silicate rainout as it is really the only set of condensates that impact the oxygen abundance. The alkali rainout discussed earlier won’t impact the metallicities and C/O ratios derived from water and methane.

⁸ Rainout likely happens for all condensates. Here we are only exploring the consequence of enstatite/forsterite rainout on the oxygen abundance

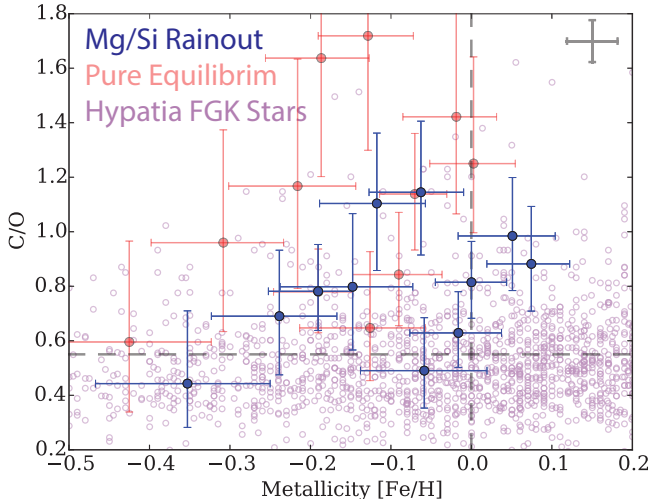


FIG. 9.— Bulk metallicity (sum of all species heavier than hydrogen and helium) and carbon-to-oxygen ratios derived from the retrieved methane and water abundances. The red points show those quantities derived from pure equilibrium. The dark blue points show those quantities derived assuming silicate rainout condensate chemistry which removed 3.28 oxygen atoms per silicon atom. This rainout effectively “depletes” the oxygen that builds water in the photosphere, resulting in a reduced water abundance relative to methane. In this regime, in order to reproduce the retrieved methane and water molecular abundances, the bulk carbon to oxygen ratios have to be lower and the metallicity higher. The data in purple was determined from the Hyatia Catalog (Hinkel et al. 2014), an amalgamate dataset of F-G-K stellar abundances, where all literature source measurements are solar normalized to Lodders et al. (2009). In the instance where multiple groups measure the same element in the same star (Hinkel et al. 2016), the median value is used for the stellar abundance and the range or *spread* of those measurements is averaged to determine how well different determinations agree, shown as the representative error bar in the top right. Our results tend to sit towards lower metallicities and higher C/O’s than the stellar population.

4.4. Evolutionary Diagnostics: Radius, Gravity, Effective Temperature, & Age

The radius, gravity, and effective temperature of a substellar object is diagnostic of its evolutionary history (Burrows et al. 2001; Saumon & Marley 2008). Late field T-dwarfs are typically expected to be high gravity ($\log g \sim 5$) and low effective temperatures, typically associated with higher ages. We find the gravities of these objects falling between 4.75 and 5.3. Gravities are not typically expected to exceed ~ 5.3 even for the oldest, most massive objects (e.g., Saumon & Marley 2008). Figure 10 summarizes the effective temperatures and gravities of the 11 objects in our sample compared with the evolution models of Saumon & Marley (2008). The retrieved gravity and radii are consistent with ages between 1 and 5 Gyr and masses between ~ 20 and 50 Jupiter radii. As an additional, more quantitative check, we use the approximate evolutionary relationships (as a function of gravity and effective temperature) from Burrows et al. (2001) (their equation 4) to derive the possible ages for each object (last column in Figure 4). Again, we find that the median ages for each object are typically greater than ~ 1 Gyr, but some span a wide range of possible ages due to the larger uncertainties on gravity. The gravity and effective temperatures of this sample are also in line with expectations from population synthesis evolutionary models (Figure 9 in Saumon & Marley 2008) for late

T-dwarfs.

The photometric radius of each object can be determined by the radius-to-distance dilution factor and photometry. This factor effectively scales the spectra uniformly in wavelength. From this scale factor, the distance, and photometry we can directly determine the radii of these objects. We find that the radii for most of the objects in our sample fall between ~ 0.7 and 1.3 Jupiter radii (Figure 4). We can test for the self-consistency of the spectroscopically derived radii using the analytic evolutionary relationship of radius with effective temperature and gravity (equation 5 in Burrows et al. 2001)⁹. Propagating the uncertainties in gravities and effective temperatures for each object into the evolutionary relationship for radius we find that our photometrically derived radii are systematically higher¹⁰ than expected from the evolution models.

The largest discrepancies (in terms of differences in the medians of the radii distributions) come from 2MASS J1553, 2MASS J1217, and to a lesser degree 2MASS J0939. As discussed in §3, from HST imagery, 2MASS J1553 has been shown to be a binary, whereas the evidence for 2MASS J1217 and 2MASS J0939 being binaries is more circumstantial, based on somewhat higher fluxes than expected based on their spectral types. In future work we if we a priori identify a binary system, or like in previous works (e.g., Burgasser et al. 2008), we identify an overly large radius, we may try fitting for the atmospheric properties of two separate objects and combining them into one spectrum (as done in Leggett et al. 2009). At this time it is unclear why discrepancies in the evolution derived radii, and the photometric radii are inconsistent. Perhaps some of these objects are indeed like 2MASS J1217 and 2MASS J0939 in they are unresolved binary systems. We encourage further imaging campaigns of discrepant systems to determine if they are indeed binaries.

We note that the recent detection of a highly irradiated ($T_{eq} \sim 2400$ K) transiting brown dwarf, KELT-1b (Siverd et al. 2012, see also Bouchy et al. 2011), also shows a larger radius, relative to evolution models, of $1.116^{+0.038}_{-0.029} R_J$ given its mass of $\sim 27 M_J$ and age ($\sim 1.5 - 2$ Gyr). However, they attribute this anomalously large radius to its high degree of stellar irradiation, driving some as-of-yet unknown inflation mechanism operating on many hot Jupiter’s (e.g., Laughlin et al. 2011). It is currently unclear how stellar irradiation driven inflation mechanisms would impact higher gravity objects ($\log g = 4 - 5$, transiting planets have $\log g < 3.5$ with most less than 3.). Bouchy et al. (2011) argue that large stellar insolation is likely to play a negligible role in increasing the radii of irradiated brown dwarf-mass objects. These measured radii are typically $\sim 10\%$ larger than expected

⁹ As a check, we compared the radii derived from the Burrows et al. (2001) equations to the “Hybrid Evolution Grid” from Saumon & Marley (2008) for relevant select T_{eff} - $\log g$ pairs. We found that for the same T_{eff} - $\log g$ pair, radii differences between the two models are no larger than $0.02 R_J$. This is small compared to the relative to the retrieved photometric radii errors of ~ 0.08 .

¹⁰ We note that the opposite is true for self-luminous directly imaged planets, as their photometrically derived radii tend to be systematically smaller than predicted from evolution models (e.g., Marley et al. 2012), possibly due to model composition assumptions.

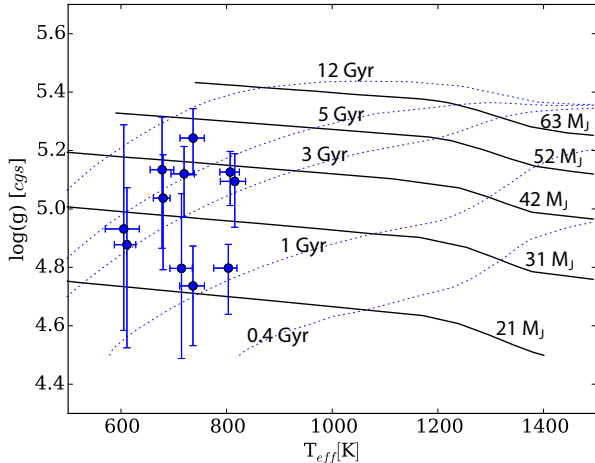


FIG. 10.— Comparison of retrieved gravities and effective temperatures with evolution models (Saumon & Marley 2008, adapted from Part I). The inferred ages (blue dashed curves) and masses (black curves) are consistent with expectations for field T-dwarfs.

tations from evolution models given their masses and a reasonable range of ages. The large radii for the non-binary systems in our sample are in good agreement with these transiting systems. However, some transiting brown dwarf mass objects, e.g., LHS 6343ABb—not highly irradiated (Johnson et al. 2011; Montet et al. 2016), do not show evidence for inflated radii ($0.833^{+0.021}_{-0.021} R_J$) and are inline with evolution model expectations. Continuing to identify these ultimate benchmark systems over a range of irradiation levels will further test evolution models and provide context for our radius determinations.

5. COMPARISON WITH PREVIOUS ANALYSIS

Table 3 summarizes our results compared with the literature. There are a wide range of literature values for effective temperatures, gravities, and radii for any individual object. In a broad sense, our results are largely in-line with what has been found before. However, we do find that in most cases our effective temperatures are systematically lower by up to $\sim 100\text{K}$, which is many sigma, when compared to previous determinations. However, the differences in the estimates from previous works can also be on the order of one to several hundred K due to different wavelength regions explored and/or different model grid. Overall, we find that our derived effective temperatures are systematically the coolest.

Our gravity determinations agree very well with previous estimates, with most previous estimates for each object falling within our 1 sigma (typically ~ 0.2 dex). The inferred metallicities are also typically in good agreement with previous determination, for select objects. For instance, for objects previously reported to have low metallicities (2MASS J0939 and ULAS J1416—our two lowest metallicity objects), we too find significantly low metallicity. We find a slightly higher, though, not significantly, metallicity for 2MASS J0415, consistent with the 0-0.3 dex determination from Saumon et al. (2007). We also find that the photometric radii are consistent with previous determinations where available (2MASS J0415 with Yamamura et al. (2010) reporting $1.14R_J$ based on

AKARI data is with 2-sigma our value of $1.06^{+0.05}_{-0.06} R_J$) and that binaries stand out as objects with overly large photometric radii (e.g., $1.26R_J$ for 2MASS J0939 from Burgasser et al. 2008, compared with our determination of $1.22^{+0.1}_{-0.09} R_J$).

6. CONCLUSIONS & DISCUSSION

We have applied the benchmark-validated retrieval methodologies of Line et al. 2015 (Part I) to low resolution near infrared spectra of a small ensemble of 11 late T-dwarfs. A systematic, uniform analysis of objects observed with the same instrument, and processed using the same modeling analysis provides a solid foundation for atmospheric property comparison and identification of diagnostic trends. We focused on late T-dwarfs in this investigation for several reasons: firstly, their spectra have a large dynamic range, directly translating into a wide range of atmospheric pressures probed; this in turn provides strong leverage on temperature-pressure profile constraints. Secondly, late T-dwarfs are largely consistent with cloud free atmospheres, mitigating a significant temperature-cloud-gas abundance degeneracy, and allowing for a vertically wide photosphere. Thirdly, the “cool” temperatures ($\sim 600\text{-}800\text{ K}$) occupied by late T-dwarfs thermochemically result in large methane and water abundances. These species are both spectrally prominent with multiple bands across the near infrared, and are the dominant carbon and oxygen reservoirs, untainted by disequilibrium chemistry, making for robust metallicity and carbon-to-oxygen ratio determinations. Finally, this temperature range encompasses the peak of the equilibrium temperatures spanned by most transiting exoplanets (Bathala et al. 2014). Understanding the physical and chemical processes in these T-dwarf laboratories, with data of similar spectral quality as the James Webb Space Telescope, will undoubtedly provide a solid foundation and context with which we can base our planetary atmosphere inferences in the not too distant future.

From this analysis, we have arrived at the following conclusions:

1. Our retrieval modeling approach can fit the data very well. The residuals are quite small and appear to be random (Figure 3).
2. Only water, methane, ammonia, and the alkalis have strong, bounded constraints (mole fractions typically constrained at 68% confidence to within ≤ 0.2 dex, or a factor of 1.6). We only obtain upper limits on the mixing ratios of the other include species (CO, CO₂, and H₂S) (Figure 4). Ammonia is present and well constrained in all objects, consistent with strong detections presented via 3 independent methods in Part I.
3. The retrieved temperature-pressure profiles are consistent with expectations from radiative-convective equilibrium temperature profiles over the photosphere (Figure 5). Deviations from grid model expectations, potentially diagnostic of additional physics, that occur outside of the photospheres should not be too heavily interpreted.

4. The retrieved molecular abundances (for the constrained species) are largely consistent with thermochemical equilibrium predictions for given temperature-pressure profile, metallicity, and carbon-to-oxygen ratio. This suggests chemical plausibility (Figure 6).
5. There is no justifiable trend in the mixing ratios of methane, water, or ammonia with effective temperature. There is however, a very strong trend in the alkali metal mixing ratios with effective temperature (Figure 7). This alkali trend is consistent with expectations from condensate rainout chemistry, which results in a depletion of the column integrated mixing ratios of elemental sodium and potassium at cooler effective temperatures as the temperature-condensate intersection pressures for Na_2S and KCl move towards the deeper atmosphere (Figure 8).
6. We only retrieve cloud optical depth upper limits. These upper limits are typically near unit optical depth (Figure 4) suggesting that clouds do not substantially influence the spectra of these 11 late T-dwarfs. This is consistent with our findings from Part I where the inclusion of cloud parameters was not justified given the data, nor did their inclusion, or lack thereof, influence in any way the constraints for the other parameters.
7. The elemental abundance analysis on the retrieved methane and water mixing ratios suggests sub-solar metallicities and somewhat super-solar carbon-to-oxygen ratios, and are somewhat lower and higher, respectively, when compared to the field F-G-K stellar abundances. One caveat being that the late T-dwarf metallicities and carbon-to-oxygen ratios are sensitive to the degree of oxygen depletion in condensates that form below the photosphere (Figure 9). More efficient oxygen depletion due to additional rainout mechanisms could further shift the metallicity and carbon-to-oxygen ratios towards solar.
8. The retrieved gravities and effective temperatures are largely consistent with evolutionary models (Figure 10) and previous works, though our retrieved effective temperatures are systematically cooler than previous grid-model derivations. We also find that the spectroscopically retrieved radii of several of the objects are larger than those expected from the evolution models derived from the retrieved effective temperatures and gravities. Some of these large radii are indicative un-resolved binary systems, consistent with the literature. The other object's larger radii are difficult to explain, but those larger radii are in line with what has been found for some transiting brown dwarfs.

We emphasize, that all of these constraints have been made with relatively low resolution spectra (SpeX Prism, at $R=80-120$). Hi-resolution is not necessarily a requirement for obtaining useful abundance information. Broad spectral coverage spanning multiple molecular bands goes a long way towards constraining molecular

abundances, even with a large number of highly degenerate parameters.

While we have learned a lot from just this small sample, there is still very much unknown and much work to be done. Expanding our sample to more objects over a wider range of temperatures will allow us to obtain better statistics on the preliminary trends presented here. We would like to first expand our sample to more low resolution spectra of late T-dwarfs and Y-dwarfs. We have demonstrated that our methodologies work within this cool temperature regime and for low-resolution data. We should understand these simpler objects before we can move onto more complex, warmer, cloudier objects (Burningham et al. in prep). As we move towards cooler temperatures, we would like to definitively identify the transition effective temperature at which we can no longer determine bounded constraints on the alkali abundances. Color-spectral type analysis suggest that this transition occurs around T8, near the Y-T transition (e.g., Schneider et al. 2015, Figure 13). Measuring the transition abundance and effective temperature would place further constraints on the rainout mechanism, and can be directly compared to equilibrium chemistry predictions. Moving towards slightly higher temperatures, we would like to identify when the strong ammonia detection disappears (becomes an upper limit), or if we can retrieve a decline in its abundance with increasing temperature (e.g., Figure 5, Burrows & Sharp 1998). The rate of decline, and where this transition occurs relative to equilibrium chemistry predictions, will place constraints on the role of disequilibrium nitrogen chemistry in late T-dwarf atmospheres (e.g., the dispersion in vertical mixing strengths).

Continued validation of the model against star-dwarf benchmark systems (like Gl570 and HD3651 from Part 1) and also dwarf-dwarf benchmark systems is also necessary to identify improvements and/or pitfalls in our current modeling. In that regards, there are several modeling improvements. Firstly, more testing and identification of robust temperature-pressure profile parameterizations are needed. Our current “p-spline smoothing prior” parameterization introduced in Part I works well for T-dwarfs, and is in agreement with expectations from self-consistent cloud-free grid models. However, cloudy objects with dampened photospheres will require less flexible parameterizations with fewer free parameters. Understanding the influence of these temperature profile assumptions on the abundances, gravities, cloud optical depths, etc., will become more important as we move towards hotter objects or objects with less spectral coverage and signal-to-noise, like self-luminous directly imaged planets. The role that various cloud parameterizations play in influencing the other retrieved properties will also need to be explored (e.g., gray non-scattering, vs. wavelength dependent scattering, cloud vertical profiles/particle sizes/compositions/patchiness, etc.), as has been done within grid modeling frameworks (e.g., Burrows et al. 2006; Cushing et al. 2008; Morley et al. 2012). Finally, more sophisticated data-model comparison techniques should be explored (e.g., Czekala et al. 2015) especially when retrieving on higher resolution spectra and stitching together spectra from different instruments, orders, and epochs. Failure to account for these direct data-model comparison subtleties may re-

sult in biased answers—a motivation for why we choose a single instrument (and mode), low resolution set of data.

Despite these challenges, we are optimistic that continued improvement and application of these retrieval methodologies to large samples of hundreds of objects spanning a wide array of temperatures, gravities, and ages, will undoubtedly provide new insights and surprises in physics and chemistry of brown dwarf atmospheres.

7. ACKNOWLEDGEMENTS

We thank Roxana Lupu and Richard Freedman for continued development and support of their extensive opacity database of which makes much of this work pos-

sible. We also thank Michael Cushing, Jackie Fahrety, Trent Dupuy, Brenden Bowler, Didier Saumon, Ryan Garland, Ty Robinson & Adam Schneider for useful discussions. M.R.L. acknowledges support provided by NASA through Hubble Fellowship grant 51362 awarded by the Space Telescope Science Institute, which is operated by the Association of Universities for Research in Astronomy, Inc., for NASA, under the contract NAS 5-26555. BB acknowledges financial support from the European Commission in the form of a Marie Curie International Outgoing Fellowship (PIOF-GA-2013- 629435). NRH acknowledges the support of the Vanderbilt Office of the Provost through the Vanderbilt Initiative in Data-intensive Astrophysics (VIDA) fellowship.

REFERENCES

- Allard, F., Hauschildt, P. H., Baraffe, I., & Chabrier, G. 1996, *ApJ*, 465, L123
- Ackerman, A. S., & Marley, M. S. 2001, *ApJ*, 556, 872
- Aitchison, J. 1986, *The statistical analysis of compositional data*, Chapman & Hall London
- Barnes, S. A. 2007, *ApJ*, 669, 1167
- Barstow, J. K., Aigrain, S., Irwin, P. G. J., Fletcher, L. N., & Lee, J.-M. 2013, *MNRAS*, 434, 2616
- Belu, A. R., Selsis, F., Raymond, S. N., et al. 2013, *ApJ*, 768, 125
- Benneke, B., & Seager, S. 2012, *ApJ*, 753, 100
- Bond, J. C., O’Brien, D. P., & Loretta, D. S. 2010, *ApJ*, 715, 1050
- Bonfanti, A., Ortolani, S., & Nascimbeni, V. 2016, *A&A*, 585, A5
- Bowler, B. P., Liu, M. C., & Dupuy, T. J. 2010, *ApJ*, 710, 45
- Burgasser, A. J. 2007, *ApJ*, 658, 617
- Burgasser, A. J., Burrows, A., & Kirkpatrick, J. D. 2006a, *ApJ*, 639, 1095
- Burgasser, A. J., Geballe, T. R., Leggett, S. K., Kirkpatrick, J. D., & Golimowski, D. A. 2006b, *ApJ*, 637, 1067
- Burgasser, A. J., et al. 2002, *ApJ*, 564, 421
- Burgasser, A. J., Kirkpatrick, J. D., Cruz, K. L., Reid, I. N., Leggett, S. K., Liebert, J., Burrows, A., & Brown, M. E. 2006c, *ApJS*, 166, 585
- Burgasser, A. J., Kirkpatrick, J. D., Reid, I. N., Brown, M. E., Miskey, C. L., & Gizis, J. E. 2003, *ApJ*, 586, 512
- Burgasser, A. J.,Looper, D., & Rayner, J. T. 2010a, *AJ*, 139, 2448
- Burgasser, A. J., Tinney, C. G., Cushing, M. C., Saumon, D., Marley, M. S., Bennett, C. S., & Kirkpatrick, J. D. 2008, *ApJ*, 689, L53
- Burgasser, A. J., et al. 1999, *ApJ*, 522, L65
- . 2000, *ApJ*, 531, L57
- . 2010b, *ApJ*, 725, 1405
- Burningham, B., et al. 2010, *MNRAS*, 404, 1952
- Burrows, A., Sudarsky, D., & Hubeny, I. 2006, *ApJ*, 640, 1063
- Burrows, A., Hubbard, W. B., Lunine, J. I., & Liebert, J. 2001, *Reviews of Modern Physics*, 73, 719
- Canty, J. I., Lucas, P. W., Yurchenko, S. N., et al. 2015, *MNRAS*, 450, 454
- Casagrande, L., Flynn, C., Portinari, L., Girardi, L., & Jimenez, R. 2007, *MNRAS*, 382, 1516
- Casagrande, L., Schönrich, R., Asplund, M., Cassisi, S., Ramírez, I., Meléndez, J., Bensby, T., & Feltzing, S. 2011, *A&A*, 530, A138
- Conrath, B. J., Gierasch, P. J., & Ustinov, E. A. 1998, *Icarus*, 135, 501
- Crisp, D., Atlas, R. M., Breon, F. M., Brown, L. R., Burrows, J. P., Ciais, P., Schroll, S. 2004, *Adv. in Space Res.*, 34, 700-709.
- Cushing, M. C., Marley, M. S., Saumon, D., et al. 2008, *ApJ*, 678, 1372
- Czekala, I., Andrews, S. M., Mandel, K. S., Hogg, D. W., & Green, G. M. 2015, *ApJ*, 812, 128
- Del Burgo, C., Martín, E. L., Zapatero Osorio, M. R., & Hauschildt, P. H. 2009, *A&A*, 501, 1059
- Dupuy, T. J., & Liu, M. C. 2011, *ApJ*, 733, 122
- . 2012, *ApJS*, 201, 19
- Faherty, J. K., et al. 2012, *ApJ*, 752, 56
- Fegley, B., Jr., & Lodders, K. 1994, *Icarus*, 110, 117
- Fernandes, J. M., Vaz, A. I. F., & Vicente, L. N. 2011, *A&A*, 532, A20
- Fischer, D. A., Butler, R. P., Marcy, G. W., Vogt, S. S., & Henry, G. W. 2003, *ApJ*, 590, 1081
- Foreman-Mackey, D., Hogg, D. W., Lang, D., & Goodman, J. 2013, *PASP*, 125, 306
- Fletcher, L. N., Irwin, P. G. J., Teanby, N. A., et al. 2007, *Icarus*, 189, 457
- Freedman, R. S., Marley, M. S., & Lodders, K. 2008, *ApJS*, 174, 504-513
- Freedman, R. S., Lustig-Yaeger, J., Fortney, J. J., et al. 2014, *ApJS*, 214, 25
- Fortney, J. J. 2012, *ApJ*, 747, L27
- Geballe, T. R., Saumon, D., Golimowski, D. A., Leggett, S. K., Marley, M. S., & Noll, K. S. 2009, *ApJ*, 695, 844
- Greathouse, T. K., Richter, M., Lacy, J., et al. 2011, *Icarus*, 214, 606
- Grimm, S. L., & Heng, K. 2015, *ApJ*, 808, 182
- Gordon, S., & McBride, B. J. 1994, *NASA Reference Publ.* 1311
- Han, C., Jung, Y. K., Udalski, A., et al. 2013, *ApJ*, 778, 38
- Heng, K., & Lyons, J. R. 2016, *ApJ*, 817, 149
- Hinkel, N. R., Timmes, F. X., Young, P. A., Pagano, M. D., & Turnbull, M. C. 2014, *AJ*, 148, 54
- Hinkel, N. R., Young, P. A., Pagano, M. D., et al. 2016, *ApJS*, 226, 4
- Hubeny, I., & Burrows, A. 2007, *ApJ*, 669, 1248
- Irwin, P. G. J., Teanby, N. A., de Kok, R., et al. 2008, *J. Quant. Spec. Radiat. Transf.*, 109, 1136
- Khandrika, H., Burgasser, A. J., Melis, C., Luk, C., Bowsher, E., & Swift, B. 2013, *AJ*, 145, 71
- Kirkpatrick, J. D. 2005, *ARA&A*, 43, 195
- Knapp, G. R., et al. 2004, *AJ*, 127, 3553
- Lee, J.-M., Fletcher, L. N., & Irwin, P. G. J. 2012, *MNRAS*, 420, 170
- Leggett, S. K., et al. 2002, *ApJ*, 564, 452
- Leggett, S. K., Marley, M. S., Freedman, R., Saumon, D., Liu, M. C., Geballe, T. R., Golimowski, D. A., & Stephens, D. C. 2007a, *ApJ*, 667, 537
- Leggett, S. K., Saumon, D., Marley, M. S., Geballe, T. R., Golimowski, D. A., Stephens, D., & Fan, X. 2007b, *ApJ*, 655, 1079
- Leggett, S. K., et al. 2009, *ApJ*, 695, 1517
- . 2010, *ApJ*, 710, 1627
- . 2012, *ApJ*, 748, 74
- Ligi, R., et al. 2016, *A&A*, 586, A94
- Line, M. R., Teske, J., Burningham, B., Fortney, J. J., & Marley, M. S. 2015, *ApJ*, 807, 183
- Line, M. R., Zhang, X., Vasisht, G., et al. 2012, *ApJ*, 749, 93
- Line, M. R., Wolf, A. S., Zhang, X., et al. 2013, *ApJ*, 775, 137
- Line, M. R., Knutson, H., Wolf, A. S., & Yung, Y. L. 2014a, *ApJ*, 783, 70
- Line, M. R., Fortney, J. J., Marley, M. S., & Sorahana, S. 2014b, *ApJ*, 793, 33
- Line, M. R., Stevenson, K. B., Bean, J., et al. 2016, *ApJ*, 152, 6
- Liu, M. C., Delorme, P., Dupuy, T. J., et al. 2011, *ApJ*, 740, 108
- Liu, M. C., Leggett, S. K., & Chiu, K. 2007, *ApJ*, 660, 1507

- Lodders, K. 1999, *ApJ*, 519, 793
- Lodders, K., & Fegley, B. 2002, *Icarus*, 155, 393
- Lodders, K., & Palme, H. 2009, *Meteoritics and Planetary Science Supplement*, 72, 5154
- Looper, D. L., Kirkpatrick, J. D., & Burgasser, A. J. 2007, *AJ*, 134, 1162
- Lucas, P. W., et al. 2010, *MNRAS*, 408, L56
- Luhman, K. L., et al. 2007, *ApJ*, 654, 570
- Mamajek, E. E., & Hillenbrand, L. A. 2008, *ApJ*, 687, 1264
- Marley, M. S., Saumon, D., Guillot, T., et al. 1996, *Science*, 272, 1919
- Marley, M. S., & Robinson, T. D. 2015, *ARA&A*, 53, 279
- McWilliam, A. 1997, *ARA&A*, 35, 503
- Metchev, S. A., et al. 2015, *ApJ*, 799, 154
- Morley, C. V., Fortney, J. J., Marley, M. S., et al. 2012, *ApJ*, 756, 172
- Mugrauer, M., Seifahrt, A., Neuhäuser, R., & Mazeh, T. 2006, *MNRAS*, 373, L31
- Payne, M. J., & Lodato, G. 2007, *MNRAS*, 381, 1597
- Petigura, E. A., & Marcy, G. W. 2011, *ApJ*, 735, 41
- Pineda, J. S., Hallinan, G., Kirkpatrick, J. D., Cotter, G., Kao, M. M., & Mooley, K. 2016, *ApJ*, 826, 73
- Patience, J., King, R. R., De Rosa, R. J., et al. 2012, *A&A*, 540, A85
- Radigan, J. 2014, *ApJ*, 797, 120
- Radigan, J., Lafrenière, D., Jayawardhana, R., & Artigau, E. 2014, *ApJ*, 793, 75
- Rice, E. L., Barman, T., Mclean, I. S., Prato, L., & Kirkpatrick, J. D. 2010, *ApJS*, 186, 63
- Rodgers, C. D. 1976, *Reviews of Geophysics and Space Physics*, 14, 609
- Rodgers, C. D. 2000, *Inverse Methods for Atmospheric Sounding - Theory and Practice*. Series: Series on Atmospheric Oceanic and Planetary Physics, ISBN: [ISBN: 9789812813718](https://doi.org/10.1142/9789812813718)/ISBN: [ISBN: 9789812813718](https://doi.org/10.1142/9789812813718). World Scientific Publishing Co. Pte. Ltd., Edited by Clive D. Rodgers, vol. 2, 2
- Saumon, D., & Marley, M. S. 2008, *ApJ*, 689, 1327
- Saumon, D., Marley, M. S., Cushing, M. C., Leggett, S. K., Roellig, T. L., Lodders, K., & Freedman, R. S. 2006, *ApJ*, 647, 552
- Saumon, D., et al. 2007, *ApJ*, 656, 1136
- Schmidt, S. J., West, A. A., Burgasser, A. J., Bochanski, J. J., & Hawley, S. L. 2010, *AJ*, 139, 1045
- Scholz, R. 2010, *A&A*, 510, L8
- Sharp, C. M., & Burrows, A. 2007, *ApJS*, 168, 140
- Sorahana, S., & Yamamura, I. 2012, *ApJ*, 760, 151
- Sorahana, S., Suzuki, T. K., & Yamamura, I. 2014, *MNRAS*, 440, 3675
- Stephens, D. C., Leggett, S. K., Cushing, M. C., et al. 2009, *ApJ*, 702, 154
- Stevenson, K. B., Bean, J. L., Madhusudhan, N., & Harrington, J. 2014, *ApJ*, 791, 36
- Teske, J. K., Cunha, K., Smith, V. V., Schuler, S. C., & Griffith, C. A. 2014, *ApJ*, 788, 39
- Testi, L. 2009, *A&A*, 503, 639
- Timmes, F. X., Woosley, S. E., & Weaver, T. A. 1995, *ApJS*, 98, 617
- Tinney, C. G., Burgasser, A. J., & Kirkpatrick, J. D. 2003, *AJ*, 126, 975
- Tinney, C. G., Burgasser, A. J., Kirkpatrick, J. D., & McElwain, M. W. 2005, *AJ*, 130, 2326
- Tremblin, P., Amundsen, D. S., Mourier, P., et al. 2015, *ApJ*, 804, L17
- Tsuji, T., Yamamura, I., & Sorahana, S. 2011, *ApJ*, 734, 73
- Tsuji, T., Ohnaka, K., Aoki, W., & Nakajima, T. 1996, *A&A*, 308, L29
- Twomey, S., Herman, B., & Rabinoff, R. 1977, *JAS*, 34, 1085
- Valenti, J. A., & Fischer, D. A. 2005, *ApJS*, 159, 141
- van Leeuwen, F. 2007, *A&A*, 474, 653
- Vican, L. 2012, *AJ*, 143, 135
- Visscher, C., Lodders, K., & Fegley, B., Jr. 2006, *ApJ*, 648, 1181
- Visscher, C., Lodders, K., & Fegley, B., Jr. 2010, *ApJ*, 716, 1060-1075
- Venn, K. A., Irwin, M., Shetrone, M. D., et al. 2004, *AJ*, 128, 1177
- Wilson, P. A., Rajan, A., & Patience, J. 2014, *A&A*, 566, A111
- Yamamura, I., Tsuji, T., & Tanabé, T. 2010, *ApJ*, 722, 682